Catalyst-like modulation of transition states for CFTR channel opening and closing: New stimulation strategy exploits nonequilibrium gating

László Csanády,[1,2] and Beáta Töröcsik[1]

[1]Department of Medical Biochemistry and [2]MTA-SE Ion Channel Research Group, Semmelweis University, Budapest H-1094, Hungary

Cystic fibrosis transmembrane conductance regulator (CFTR) is the chloride ion channel mutated in cystic fibrosis (CF) patients. It is an ATP-binding cassette protein, and its resulting cyclic nonequilibrium gating mechanism sets it apart from most other ion channels. The most common CF mutation (ΔF508) impairs folding of CFTR but also channel gating, reducing open probability (P_o). This gating defect must be addressed to effectively treat CF. Combining single-channel and macroscopic current measurements in inside-out patches, we show here that the two effects of 5-nitro-2-(3-phenylpropylamino)benzoate (NPPB) on CFTR, pore block and gating stimulation, are independent, suggesting action at distinct sites. Furthermore, detailed kinetic analysis revealed that NPPB potently increases P_o, also of ΔF508 CFTR, by affecting the stability of gating transition states. This finding is unexpected, because for most ion channels, which gate at equilibrium, altering transition-state stabilities has no effect on P_o; rather, agonists usually stimulate by stabilizing open states. Our results highlight how for CFTR, because of its unique cyclic mechanism, gating transition states determine P_o and offer strategic targets for potentiator compounds to achieve maximal efficacy.

The Journal of General Physiology

INTRODUCTION

CFTR is a chloride ion channel (Bear et al., 1992) crucial for the salt water balance of several polarized epithelia. Mutations in CFTR are the cause of cystic fibrosis (CF) (Riordan et al., 1989), the most common lethal genetic disease among Caucasians, an incurable, devastating multi-organ disorder (O'Sullivan and Freedman, 2009). The most common CF-causing mutation (carried by >90% of patients), deletion of phenylalanine 508 (ΔF508), severely impairs both protein folding/stability (Cheng et al., 1990; Okiyoneda et al., 2010; Rabeh et al., 2012) and channel open probability (P_o) (Wang et al., 2005; Miki et al., 2010). Thus, much effort is focused on the development of "correctors," chemical chaperones that promote folding/stability of the ΔF508 CFTR protein, and of "potentiators," which stimulate P_o of ΔF508 (or other mutant) CFTR channels.

CFTR is an ATP-binding cassette (ABC) protein, with a typical ABC architecture consisting of two transmembrane domains (TMDs) and two cytosolic nucleotide-binding domains (NBDs). The additional cytosolic regulatory (R) domain, unique to CFTR (Riordan et al., 1989), is a substrate for cyclic AMP-dependent PKA, and its phosphorylation is required for CFTR channel activity (Tabcharani et al., 1991). CFTR's chloride ion pore is formed by the TMDs and gated by a cycle of ATP binding and hydrolysis at the two NBDs (Gadsby et al., 2006).

Despite the functional divergence of the ion channel CFTR from other ABC proteins, which are mainly active transporters, a conserved molecular mechanism couples cycles of conformational changes in NBDs and in TMDs of all ABC proteins (Locher, 2009). In the presence of ATP, NBDs of ABC proteins form tight head-to-tail dimers, occluding two molecules of ATP; each nucleotide is sandwiched between the conserved Walker A and B motifs of one NBD and the conserved signature sequence of the other, which together form a composite catalytic site with ATPase activity (e.g., Karpowich et al., 2001; Smith et al., 2002). NBD dimers glued together by two ATP molecules are extremely stable, but they dissociate after ATP hydrolysis (Moody et al., 2002; Verdon et al., 2003). In ABC-C family members, including CFTR (ABCC7), the composite binding site formed by Walker motifs of NBD1 and signature sequence of NBD2 ("site 1") is degenerate and catalytically inactive (Aleksandrov et al., 2002; Basso et al., 2003); ATP hydrolysis occurs only in "site 2" (formed by Walker motifs of NBD2 plus signature sequence of NBD1). In full-length ABC exporter structures, tightly associated NBD dimers are linked with outward-facing (Dawson and Locher, 2006; Ward et al., 2007) and fully or partially separated

Correspondence to László Csanády: csanady.laszlo@med.semmelweis-univ.hu

Abbreviations used in this paper: ABC, ATP-binding cassette; CF, cystic fibrosis; NBD, nucleotide-binding domain; NPPB, 5-nitro-2-(3-phenylpropylamino)benzoate; P_o, open probability; TMD, transmembrane domain.

The Rockefeller University Press $30.00
J. Gen. Physiol. Vol. 143 No. 2 269–287
www.jgp.org/cgi/doi/10.1085/jgp.201311089

NBDs with inward-facing (Ward et al., 2007; Aller et al., 2009; Hohl et al., 2012) TMD conformations, suggesting that formation of ATP-bound NBD dimers flips the TMDs from inward to outward facing, whereas ATP hydrolysis drives dimer dissociation to reset the TMDs to inward facing (Locher, 2009).

In the ion channel CFTR, the NBD dimerization–dissociation cycle is coupled to the opening and closure of the transmembrane permeation pathway: the pore opens to a burst when the tight NBD dimer forms, and it closes from a burst when the dimer interface separates around site 2, after hydrolysis of the ATP bound there (Vergani et al., 2005). (CFTR current records display a bursting pattern: open events, which last for ∼2–300 ms, are interrupted by brief [<10-ms] ATP-independent "flickery" closures, distinct from the long closed events [∼1 s] that reflect NBD dimer separation ["interburst closures"; Vergani et al., 2003]; in this study, the terms "pore opening" and "pore closure" are used synonymously with entering and exiting a burst.) In the absence of hydrolysis, pore closure is extremely slow: site-2 mutations that disrupt ATP hydrolysis slow the closing rate by ∼100-fold (Gunderson and Kopito, 1995). Thus, gating of WT channels is an essentially unidirectional cycle; channels that open to a prehydrolytic open state (O_1) preferentially progress to a post-hydrolytic open state (O_2), to then close through a pathway ($O_2 \rightarrow C_2$) distinct from pore opening ($C_1 \rightarrow O_1$) (shown in insets throughout Figs. 3–5; Csanády et al., 2010). This far-from-equilibrium operation is rare among ion channels but is an essential property of ABC transporters that mediate unidirectional uphill transport. At saturating [ATP], the CFTR functional cycle contains two rate-limiting steps with relatively high free energy barriers: step $C_1 \rightarrow O_1$ (rate of $\sim 1\ s^{-1}$) determines opening rate, whereas step $O_1 \rightarrow O_2$ (rate of $\sim 4\ s^{-1}$) rate limits closure (Csanády et al., 2010).

Because the TMDs are the most divergent parts of ABC proteins, they are promising targets for the development of highly selective drugs. The arylaminobenzoate 5-nitro-2-(3-phenylpropylamino)benzoate (NPPB) is an anionic compound that binds to CFTR's TMDs, and it has been studied extensively for its pore blocker properties (Zhang et al., 2000; Zhou et al., 2010). Unexpectedly, Wang et al. (2005) discovered that NPPB, in addition to blocking the pore, dramatically increases P_o (i.e., potentiates gating) of both WT and ΔF508 CFTR. Given the potential therapeutic impact of CFTR potentiators, the present study aimed to identify the exact molecular mechanism by which NPPB stimulates P_o. As a control, we compared the effects of NPPB to those of MOPS, another well-characterized CFTR pore blocker (Ishihara and Welsh, 1997), but without potentiating effects. Our results offer a conceptually novel approach to robustly stimulate CFTR that exploits its unique nonequilibrium gating cycle, and that differs fundamentally from strategies applied so far to modulate the activity of any ion channel.

MATERIALS AND METHODS

Molecular biology

WT and mutant CFTR cDNA in pGEMHE was transcribed in vitro using T7 polymerase, and 0.1–10 ng cRNA was injected into *Xenopus laevis* oocytes as described previously (Csanády et al., 2010).

Electrophysiology

Current recordings were done at 25°C in inside-out patches excised from oocytes 2–3 d after RNA injection. Pipette solution contained (mM): 136 NMDG-Cl, 2 $MgCl_2$, and 5 HEPES, pH 7.4 with NMDG. Bath solution (mM: 134 NMDG-Cl, 2 $MgCl_2$, 5 HEPES, and 0.5 EGTA, pH 7.1 with NMDG) was continuously flowing and could be exchanged with a time constant of 20–30 ms. CFTR channels were prephosphorylated by 1–2-min exposure to 300 nM PKA catalytic subunit (Sigma-Aldrich). Recordings were done in the presence of saturating (2 mM) MgATP; for the K1250A mutant 10 mM MgATP was used to compensate for its greatly impaired apparent ATP affinity (Vergani et al., 2003). MgATP (Sigma-Aldrich) was added from a 400-mM aqueous stock solution (pH 7.1 with NMDG), and Na_4-pyrophosphate was added from a 500-mM aqueous stock solution, together with equimolar $MgCl_2$. NPPB (Sigma-Aldrich) was added from a 250-mM stock solution in DMSO; by spectrophotometry, NPPB solubility in water was >400 µM. Solutions containing MOPS were adjusted to pH 7.2; thus, [$MOPS^-$] was ∼50% of total [MOPS] (pK_a = 7.2). Currents recorded (Axopatch 200B; Molecular Devices) at a bandwidth of 2 kHz were digitized at 10 kHz (Digidata 1322A; Pclamp9; Molecular Devices).

Data analysis

For gating analysis, current records were refiltered at 100 Hz. Steady-state mean burst and interburst durations in patches containing fewer or equal to two channels (Fig. 6 F) were obtained by maximum likelihood fits of the closed-open-blocked scheme to the ensembles of all dwell-time histograms (Csanády, 2000); this approach efficiently separates brief ATP-independent "flickery" closures from long "interburst" closed events (Csanády et al., 2010). For burst analysis of one-channel records (Fig. 5), brief closures were suppressed using the method of Jackson et al. (1983). Distributions of burst durations longer than t_{low} = 12 ms were fitted to gating models by maximum likelihood (Csanády et al., 2010); alternative models were compared using the log-likelihood ratio test (Csanády, 2006). Average unitary current amplitudes were estimated from Gaussian fits to amplitude histograms of heavily (10 Hz) filtered records (see Fig. 1 B).

Fitting of pH titrations

Because titration of NPPB (Fig. 9 A) had to be done in a dilute (100-µM) solution, the titration curve was fitted by accounting for the presence of ∼10 µM of aqueous CO_2. Thus, the data were fitted to a curve expected for a mixture of two weak acids: for one component (CO_2) a fixed concentration of 10 µM and pK_a^* = 6.47 was used, whereas concentration and pK_a of the second component (NPPB) was left free during the fit. The slight deviation of the data from the fitted curve at pH >9 (Fig. 9 A) reflects inevitable progressive accumulation of dissolved CO_2 at very basic pH.

Statistics

All symbols and bars represent the mean ± SEM of at least five measurements, obtained from several patches. For parameters extracted from macroscopic currents, the average number of measurements was greater than nine, and the average number of patches was greater than five, for each data point (bar or symbol) shown. For the single-channel data shown in Figs. 5 and 6 F, the numbers of patches analyzed for each condition are provided in

the figure legends. Statistical significance was evaluated using Student's two-tailed *t* test (*, $P < 0.05$; **, $P < 0.01$).

Online supplemental material

Fig. S1 illustrates the kinetics of pore block by NPPB and MOPS. Fig. S2 demonstrates the effect of NPPB on the unlocking rate of WT CFTR channels locked open by ATP plus pyrophosphate. The online supplemental material is available at http://www.jgp.org/cgi/content/full/jgp.201311089/DC1.

RESULTS

Voltage-dependent pore block by NPPB and MOPS reduces average unitary current through bursting CFTR channels

Cytosolic anionic pore blockers are driven into the CFTR pore by hyperpolarizing voltages and disrupt the flow of chloride ions, causing flickery block. To deconvolve

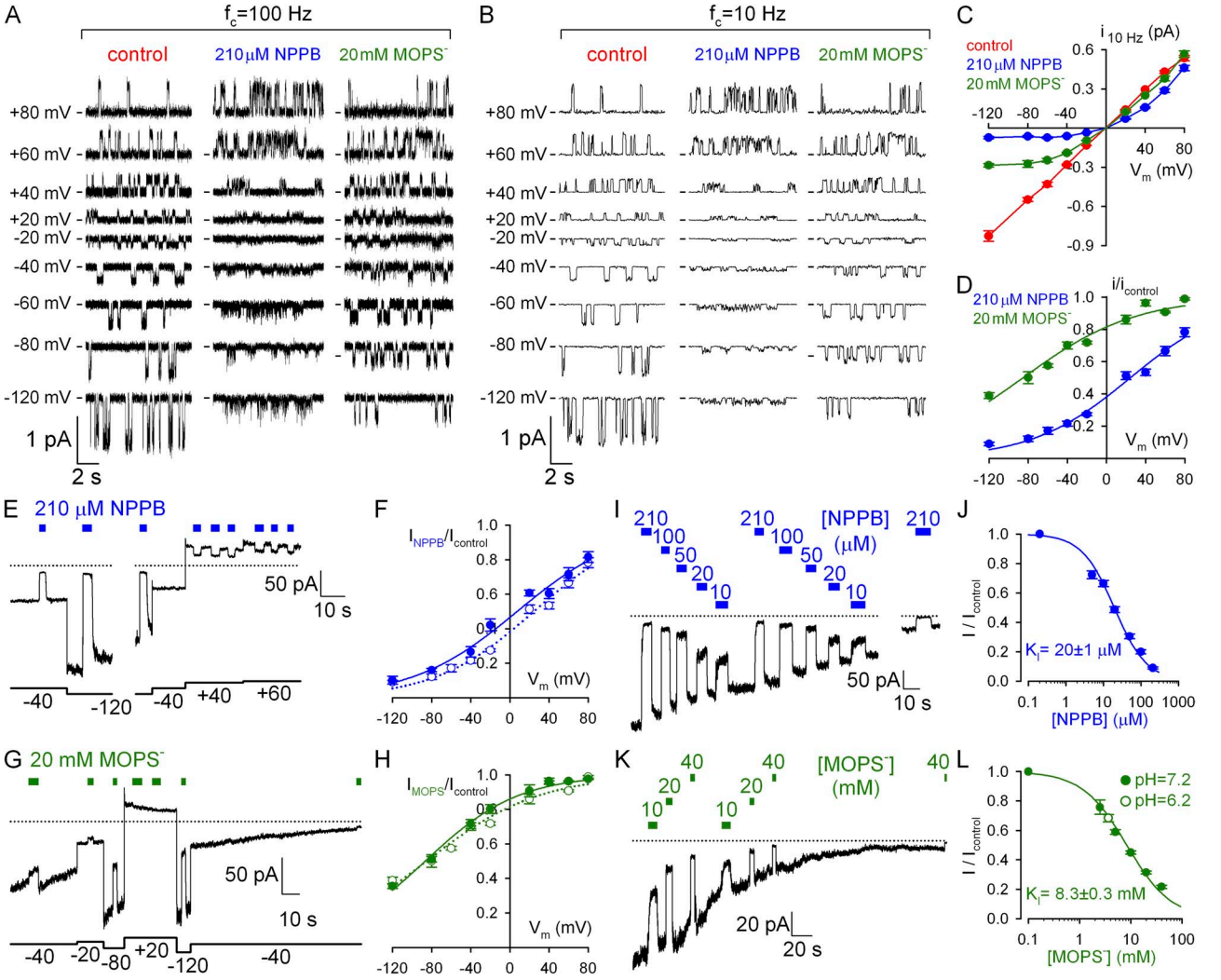

Figure 1. Voltage and dose dependence of pore block by NPPB and $MOPS^-$. (A and B) Unitary WT CFTR currents in symmetrical ~140-mM Cl^- with and without cytosolically applied blockers, displayed at two bandwidths (f_c, filter corner frequency). We could not reliably discern two distinct conductance levels in $MOPS^-$ (Gunderson and Kopito, 1995). (C) Apparent unitary amplitudes at 10 Hz, with and without blockers, plotted against voltage. (D) Fractional unitary current in 210 µM NPPB and 20 mM $MOPS^-$ (symbols) and Boltzmann fits (solid lines); midpoint voltages ($V_{1/2}$) and apparent valences (z) were $V_{1/2} = -85 \pm 3$ mV and $z = -0.45 \pm 0.03$ for $MOPS^-$ and $V_{1/2} = 24 \pm 2$ mV and $z = -0.51 \pm 0.03$ for NPPB. (E, G, I, and K) Slowly decaying macroscopic "locked-open" currents of E1371S CFTR in the absence of bath ATP; brief applications of 210 µM NPPB or 20 mM $MOPS^-$ at various voltages (E and G) or of various blocker concentrations at −120 mV (I and K). Dotted lines show zero-current levels estimated from final segments; in E and G, small (<1 pA/40 mV) linear seal currents were subtracted. (F and H) Voltage dependence of macroscopic current block by (F) 210 µM NPPB and (H) 20 mM $MOPS^-$ (closed symbols) and Boltzmann fits (solid lines); $V_{1/2} = -87 \pm 3$ mV and $z = -0.54 \pm 0.07$ for $MOPS^-$ and $V_{1/2} = 7 \pm 3$ mV and $z = -0.48 \pm 0.03$ for NPPB; open symbols and dotted lines replotted from panel D. (J and L) Dose dependence of macroscopic current block by (J) NPPB and (L) $MOPS^-$ at −120 mV (closed symbols) and Michaelis–Menten fits (solid lines). Open symbol in L: block by 40 mM of total MOPS (MOPS-H plus $MOPS^-$) at pH 6.2; calculated $[MOPS^-] = 3.6$ mM: fractional block by MOPS depends on $[MOPS^-]$, not total [MOPS], confirming anionic $MOPS^-$ to be responsible for pore block (Ishihara and Welsh, 1997).

effects on gating from those on permeation (pore block), we first quantitated the latter in inside-out patches of single WT CFTR channels gating in 2 mM of bath ATP (Fig. 1 A, left). Bath application of 210 µM NPPB elicited flickery closures whose frequency increased at more negative potentials to such an extent that distinct unitary gating events disappeared, leaving "fuzzy" noise (Fig. 1 A, middle). In contrast, bath application of 20 mM $MOPS^-$ appeared to reduce unitary current amplitudes at negative voltages (Fig. 1 A, right). This seemingly different behavior reflects the lower affinity of $MOPS^-$ for the CFTR pore, resulting in briefer interactions and hence blocked events too fleeting to be resolved at our recording bandwidth of 100 Hz (Fig. S1; Ishihara and Welsh, 1997; Zhang et al., 2000). On the other hand, after filtering the data at 10 Hz (Fig. 1 B), the effect of NPPB on unitary currents appears similar to that of $MOPS^-$; both appear to reduce unitary amplitudes at negative voltages. For the purposes of this study, it is useful to describe pore block in terms of a reduction of average unitary chloride current (i) flowing through the open pore (Fig. 1 C; compare blue and green to red symbols), as observed in heavily filtered (10-Hz) records. Plotting fractional unitary currents in the presence of NPPB or $MOPS^-$ against membrane voltage (Fig. 1 D) revealed, despite different affinities, similar voltage dependence of pore block: effective valences (from Boltzmann fits; Fig. 1 D, solid lines) were -0.51 ± 0.03 for NPPB and -0.45 ± 0.03 for $MOPS^-$ (compare to Ishihara and Welsh, 1997), suggesting that both blocking sites sense ~50% of the transmembrane electrical field.

A convenient macroscopic pore block assay is afforded by the nonhydrolytic E1371S CFTR mutant, which lacks the catalytic glutamate in site 2. These channels open rapidly in response to ATP but stay open for tens of seconds (Vergani et al., 2003), consistent with defective ATP hydrolysis. Because they are active in resting cells (compare to Zhou et al., 2010), excision of E1371S multichannel patches into an ATP-free solution typically uncovers large, slowly decaying currents devoid of gating fluctuations (Fig. 1, E, G, I, and K). As they flow through virtually locked open channels (P_o of ~1), responses of such currents to brief (2–5-s) applications of blockers reflect pure pore block. Indeed, brief applications of 210 µM NPPB (Fig. 1 E) or 20 mM $MOPS^-$ (Fig. 1 G) at various voltages yielded voltage-dependent current block (Fig. 1, F and H, closed symbols and lines), which essentially replicated the effects on unitary current amplitudes (Fig. 1, F and H, open symbols and dotted lines; replotted from Fig. 1 D). Using this convenient methodology, we measured pore block at varying [NPPB] (Fig. 1 I) and [$MOPS^-$] (Fig. 1 K) at a fixed voltage of −120 mV, constructed dose–response curves (Fig. 1, J and L), and obtained apparent K_I values of ~20 µM for NPPB (compare to Zhang et al., 2000) and ~8 mM for $MOPS^-$ (compare to Ishihara and Welsh, 1997).

Comparison of effects on macroscopic and unitary currents reveals potent gating stimulation by NPPB but not $MOPS^-$

We next examined the effects of NPPB and $MOPS^-$ on macroscopic currents of WT CFTR channels opening and closing at steady state in saturating (2 mM) ATP. At −120 mV, the application of increasing [NPPB] (Fig. 2 A) or [$MOPS^-$] (Fig. 2 C) inhibited these currents in a dose-dependent manner, and fractional inhibition by $MOPS^-$ (Fig. 2 D, closed symbols; K_I of ~15 mM) was reasonably explained by its effect on unitary currents (Fig. 2 D, open symbols; replotted from Fig. 1 L). In contrast, for NPPB (Fig. 2 B), at any given concentration, the fractional reduction of macroscopic WT steady-state currents (closed symbols) was milder than

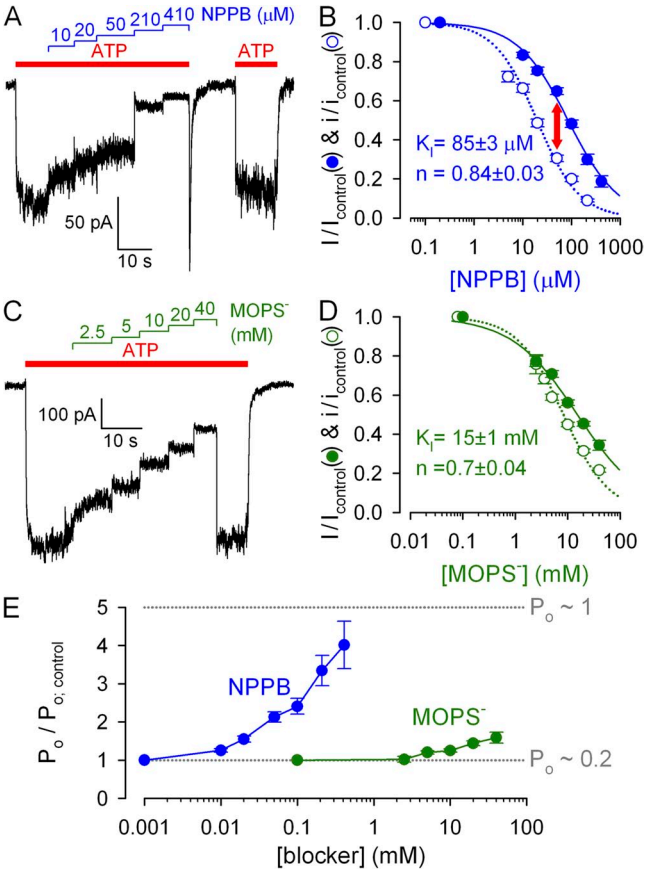

Figure 2. Discrepancy between macroscopic and unitary effects on WT CFTR quantifies gating stimulation. (A and C) Dose-dependent inhibition by cytosolic NPPB (A) and $MOPS^-$ (C) of steady-state macroscopic WT CFTR currents in 2 mM ATP at −120 mV. (B and D) Dose dependence of fractional currents in (B) NPPB and (D) $MOPS^-$ at −120 mV (closed symbols), and Hill fits (solid lines); open symbols and dotted lines show dose dependence of pore block, replotted from Fig. 1 (J and L). (E) Gating stimulation by NPPB and $MOPS^-$ at −120 mV; $P_o/P_{o;\,control}$ was calculated as the ratio $(I/I_{control}):(i/i_{control})$.

the fractional reduction of unitary currents (open symbols; replotted from Fig. 1 J), yielding an apparent K_I of ~85 µM (compare to Zhang et al., 2000).

The macroscopic current (I) is given by $I = N \cdot i \cdot P_o$, where N is the number of channels in the patch, i is understood as average unitary current during a burst, and P_o is the fraction of time a channel spends in the bursting state (bursting probability). Therefore, a discrepancy between fractional effects of a drug on i and I (Fig. 2 A, red arrow) indicates that the drug must also simultaneously affect P_o. The fractional effect on P_o (Fig. 2 E) is given by the ratio of normalized macroscopic and unitary currents. A marginal increase in P_o (~50%) was observed in very high (≥20 mM) $MOPS^-$ (Fig. 2 E, green symbols). But a much more potent gating stimulation was seen with NPPB, at submillimolar concentrations, with P_o increased up to fourfold (Fig. 2 E, blue symbols): a close-to-maximal stimulation, considering that P_o is ~0.2 under control conditions (see Fig. 5 B).

NPPB speeds opening and slows closure of WT CFTR channels

To understand the mechanism by which NPPB increases P_o, we systematically studied its effects on the rates of individual steps in the gating cycle (Fig. 3 C, cartoon). We first examined effects on the rate of normal, hydrolytic closure of WT CFTR (Fig. 3 C, cartoon, purple arrow; r_{OC}) by comparing macroscopic current relaxation rates (at −120 mV) upon sudden ATP removal in the absence or presence of 210 µM NPPB (Fig. 3 A). Single-exponential fits (Fig. 3 A, solid lines, time constants indicated) revealed approximately fourfold slower closing rates in the presence of 210 µM NPPB relative to control (Fig. 3 C, blue vs. red bar). In contrast, in similar experiments, 20 mM $MOPS^-$ (Fig. 3 B) failed to alter channel closing rate (Fig. 3 C, green bar).

To evaluate a potential effect of NPPB on opening rate, we exposed WT CFTR channels gating at steady state in 2 mM ATP to 210 µM NPPB (Fig. 3 D). Although in similar experiments $MOPS^-$ application and removal

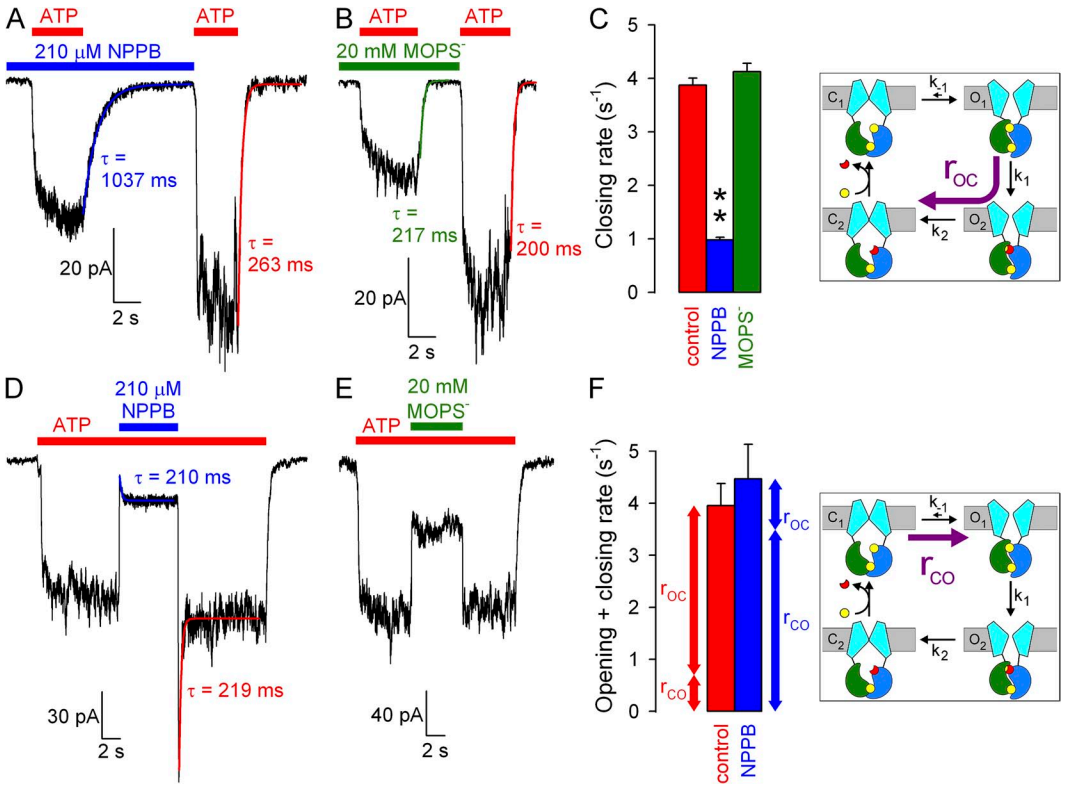

Figure 3. Effects of NPPB and $MOPS^-$ on WT CFTR opening and closing rate. (A and B) Macroscopic WT CFTR currents at −120 mV elicited by brief exposures to 2 mM ATP in the absence or presence of (A) 210 µM NPPB or (B) 20 mM $MOPS^-$; colored lines, single-exponential fits (τ, time constants). (C) Macroscopic closing rates (bars, $r_{OC} = 1/\tau$) in the absence (red) and presence of NPPB (blue) or $MOPS^-$ (green). (D and E) Macroscopic WT CFTR currents in 2 mM ATP at −120 mV, and brief exposure to (D) 210 µM NPPB or (E) 20 mM $MOPS^-$. Colored lines in D, single-exponential fits. (F) Sums of opening and closing rates in the absence and presence of NPPB ($1/\tau$ from D); opening rates (r_{CO}, bottom vertical arrows) are estimated by subtraction of closing rates (r_{OC}, top vertical arrows; see C) from the sums. Cartoons in C and F (also in Figs. 4, B and E, and 5, B and E) depict simplified cyclic CFTR gating model: cyan, TMDs; green, NBD1; blue, NBD2; yellow, ATP; red, ADP. Purple arrows highlight the pathway under study.

caused simple monophasic current relaxations (Fig. 3 E), both the addition and removal of NPPB elicited biphasic responses (Fig. 3 D), attesting to the dual effects of this compound. Upon NPPB application, instantaneous (τ of ~20 ms, reflecting solution exchange time) pore block was followed by a partial current recovery, as a larger pool of channels was drawn into the open burst state. Upon NPPB withdrawal, instantaneous relief from pore block revealed this larger pool of open channels in the form of a large current overshoot, which then relaxed back to the pre-application steady-state current level. The rate of macroscopic current relaxation after a sudden change in gating parameters reflects the sum of the average microscopic opening and closing rates in the new conditions. Interestingly, single-exponential fits to the current time courses after block (Fig. 3 D, blue fit line) and unblock (red fit line) yielded similar time constants, suggesting that the sum of opening and closing rates in the presence (Fig. 3 F, blue bar) and absence (Fig. 3 F, red bar) of 210 µM NPPB is not very different. However, in the absence of NPPB, this sum is largely dominated by the closing rate (compare Fig. 3 F, red bar, to Fig. 3 C, red bar). In contrast, in the presence of NPPB, closing rate is slowed to ~1 s^{-1} (Fig. 3 C, blue bar); thus, the sum (Fig. 3 F, blue bar) must be dominated by an increased opening rate (see also Fig. 6 D). These data suggest that NPPB increases channel opening rate, which, under our conditions of saturating ATP, reflects the rate of step $C_1 \rightarrow O_1$ (Fig. 3 F, cartoon, purple arrow; r_{CO}).

In a nonhydrolytic CFTR mutant, NPPB speeds gating but does not affect P_o

For most ion channels, potentiators stabilize open states. If NPPB acted by stabilizing state O_1 relative to C_1, then, in addition to speeding opening (see Fig. 3 F), it might be expected to slow the reverse of the opening step, i.e., nonhydrolytic closure (Fig. 4 B, cartoon, purple arrow; k_1). To test this, we studied the closing rate of K1250A CFTR channels, in which mutation of the NBD2 Walker A lysine abrogates ATP hydrolysis at site 2 (Ramjeesingh et al., 1999) and reduces gating to reversible

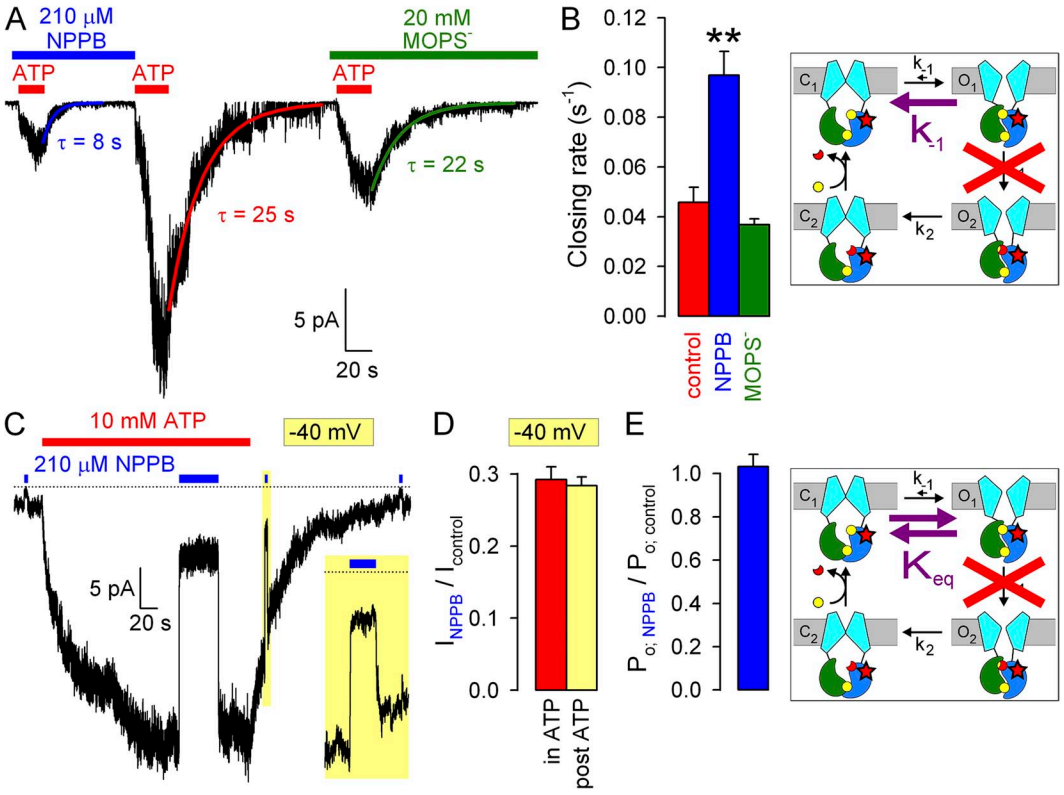

Figure 4. Effects of NPPB and $MOPS^-$ on gating rates under nonhydrolytic conditions. (A) Macroscopic K1250A CFTR current at −120 mV elicited by exposures to 10 mM ATP in the absence or presence of blockers. Colored lines, single-exponential fits (τ, time constants). (B) Macroscopic closing rates (bars, $1/\tau$) in the absence (red) and presence of NPPB (blue) or $MOPS^-$ (green) quantify effects on rate k_1 (cartoon, purple arrow). The K1250A mutation (B and E, cartoons, red stars) disrupts ATP hydrolysis in site 2 (red cross). (C) Macroscopic K1250A CFTR current elicited by 10 mM ATP at −40 mV, prolonged exposure to 210 µM NPPB of channels gating at steady state, and brief exposure to NPPB of surviving locked-open channels after ATP removal (10-s yellow box, expanded in inset). Bracketing brief applications of NPPB to small residual CFTR currents were used to estimate zero-current level (dotted line). (D) Fractional K1250A CFTR currents at −40 mV in 210 µM NPPB applied during steady-state gating (red bar) or in the locked-open state (yellow bar). (E) Effect of NPPB on the closed–open equilibrium (cartoon, purple double arrow). Fractional effect on P_o for K1250A CFTR (blue bar) was calculated as in Fig. 2 E.

$C_1 \leftrightarrow O_1$ transitions (Fig. 4 B, cartoon). Consistent with previous reports (Gunderson and Kopito, 1995; Vergani et al., 2003; Csanády et al., 2010), macroscopic closing rate of K1250A upon removal of bath ATP (Fig. 4 A) was ~100 times slower than for WT channels (Fig. 4, A, red fit line, and B, red bar; compare to Fig. 3, A and C). Whereas 20 mM $MOPS^-$ did not affect nonhydrolytic closure (Fig. 4, A, green fit line, and B, green bar), 210 µM NPPB unexpectedly accelerated it by two- to threefold (Fig. 4, A, blue fit line, and B, blue bar). As an alternative approach for studying effects on nonhydrolytic closure, we also compared unlocking rates in the absence and presence of NPPB for WT CFTR channels locked in the open state by exposure to a mixture of ATP plus pyrophosphate (Gunderson and Kopito, 1994; Tsai et al., 2009). Consistent with its effect on K1250A closing rate (Fig. 4, A and B), 210 µM NPPB also accelerated the unlocking rate of pyrophosphate-locked WT CFTR channels by two- to threefold (Fig. S2).

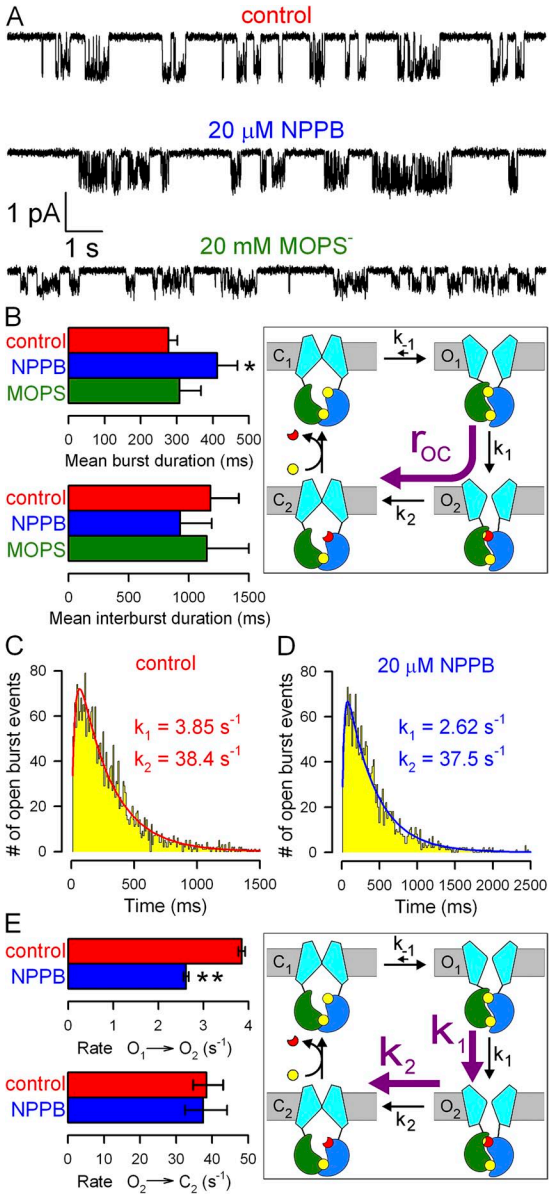

Figure 5. Effects of NPPB and $MOPS^-$ on WT CFTR microscopic steady-state gating parameters. (A) Currents from single WT CFTR channels at −120 mV in 2 mM ATP ± blockers; bandwidth, 100 Hz. (B) Mean burst (τ_b) and interburst (τ_{ib}) durations (bars) in 2 mM ATP (red), 2 mM ATP plus 20 µM NPPB (blue), and 2 mM ATP plus 20 mM $MOPS^-$ (green); closing rate (cartoon, purple arrow) is $1/\tau_b$. Bars were generated from data originating from 15, 10, and 9 patches, respectively, for the control, NPPB, and MOPS conditions; error bars represent SEM. (C and D) Dwell-time histograms of burst durations of WT CFTR channels at −120 mV in 2 mM ATP (C; 2,999 bursts, pooled from 15 patches) or 2 mM ATP plus 20 µM NPPB (D; 2,069 bursts, pooled from 10 patches) and maximum likelihood fits (solid lines) to the scheme cartooned in E (with k_1 fixed to zero). (E) Estimates of rates k_1 (step $O_1 \rightarrow O_2$) and k_2 (step $O_2 \rightarrow C_2$) in ATP and ATP plus 20 µM NPPB. Asymmetric error bars represent 0.5-unit log-likelihood intervals.

Because NPPB accelerated both forward (Fig. 3 F) and backward (Fig. 4 B) transitions of the $C_1 \leftrightarrow O_1$ step, we examined whether it affects the equilibrium constant between those two states (Fig. 4 E, cartoon, purple double arrow; K_{eq}), i.e., P_o for K1250A channels. Even prolonged exposure to 210 µM NPPB of K1250A channels gating at steady state in 10 mM ATP (Fig. 4 C; note $V_m = -40$ mV) failed to elicit biphasic responses like those seen for WT channels (see Fig. 3 D). Moreover, fractional current inhibition at steady state was identical to that instantaneously observed upon brief application of NPPB long after ATP removal (Fig. 4 C, yellow box, expanded in inset). The latter maneuver measures pure pore block of surviving open channels, i.e., fractional reduction of *i* (see Fig. 1, E, G, I, and K). The very similar fractional NPPB effects under those two conditions (Fig. 4 D, red vs. yellow bar; compare to Fig. 2 B) revealed no fractional change in P_o (Fig. 4 E, blue bar). Thus, in contrast to its effect on hydrolytic gating (Fig. 2 E), NPPB does not affect P_o for steady-state nonhydrolytic gating. Given the observed increase in nonhydrolytic closing rate (Fig. 4, A and B), this result indicates that NPPB must also speed the opening rate of K1250A CFTR, just as it does for WT (Fig. 3 F). The magnitude of the NPPB effects on opening and closing rates must be similar, such that the $C_1 \leftrightarrow O_1$ equilibrium constant is not affected; i.e., by reducing the height of the energetic barrier separating the two states, NPPB acts as a catalyst for this step.

NPPB slows WT CFTR closure by slowing the ATP-hydrolysis step

NPPB slowed the hydrolytic closing rate of WT CFTR (Fig. 3, A and C), which reflects sequential transition through the prehydrolytic O_1 and post-hydrolytic O_2 states (Fig. 3 C, cartoon, purple arrow; r_{OC}). Dissection of the rates of the two sequential steps requires maximum likelihood fitting of the distributions of open burst durations (Csanády et al., 2010). To achieve this,

we analyzed steady-state gating of single WT CFTR channels under control conditions, in 20 µM NPPB (unitary currents in 210 µM NPPB could not be resolved at −120 mV [Fig. 1 A], whereas 20 µM NPPB did not compromise reliable event detection), or in 20 mM $MOPS^-$ (Fig. 5 A). 20 mM $MOPS^-$ did not significantly affect either mean burst (308 ± 60 ms; $n = 9$) or mean interburst durations (Fig. 5 B, green bars). However NPPB, even at this low concentration, significantly prolonged mean burst duration (from 277 ± 24 ms [$n = 37$] to 412 ± 56 ms [$n = 15$]; P = 0.013), i.e., slowed closure; reduction of mean interburst duration was not significant (Fig. 5 B, blue vs. red bars).

To determine which of the two sequential closing steps is slowed by NPPB, we reconstructed the distributions of burst durations for single WT CFTR channels gating at −120 mV in the absence (Fig. 5 C) or presence of 20 µM NPPB (Fig. 5 D). Both distributions were peaked and fit (Fig. 5, C and D, solid lines) significantly better ($P = 4 \times 10^{-12}$ and 9×10^{-7}, respectively, by the log-likelihood ratio test) by the two-parameter (k_1, k_2) irreversible sequential closing mechanism (Fig. 5 E, cartoon, purple arrows) than by a single exponential. The fit parameters (Fig. 5 E, bars) attested to a significant ($P < 10^{-4}$) reduction by NPPB of the slow rate k_1, which represents the rate of step $O_1 \rightarrow O_2$ associated with ATP hydrolysis in site 2 (Csanády et al., 2010).

Voltage-independent gating stimulation by NPPB suggests distinct binding sites for pore block and gating effects

NPPB was first identified as a potentiator at positive voltages (Wang et al., 2005) because at negative voltages gating stimulation is masked by the pore block, which is voltage dependent. To assess whether any of its effects on gating are also voltage dependent, we systematically studied gating in NPPB at +60 mV and compared NPPB effects at +60 mV with those at −120 mV (Figs. 1–4). Because at positive voltages unitary current in 210 µM NPPB remains ∼67% of control (as opposed to ∼9% at −120 mV; Fig. 1 D), gating stimulation prevails over pore block, causing dose-dependent overall stimulation of macroscopic WT CFTR current (Fig. 6 A). Indeed, dividing fractional macroscopic currents (Fig. 6 B, open squares) by fractional unitary currents (Fig. 6 B, open diamonds) revealed a powerful increase in P_o (Fig. 6 B, closed circles); the approximately threefold stimulation by 210 µM NPPB approached that observed at −120 mV (Fig. 2 E, blue circles). Furthermore, 210 µM NPPB slowed closing rate by approximately threefold (Fig. 6 C; compare to Fig. 3, A and C), and similar macroscopic relaxation rates upon the addition and removal of NPPB attested to a simultaneous increase in opening rate in the presence of NPPB (Fig. 6 D; compare to Fig. 3, D and F). Finally, at +60 mV, 210 µM NPPB increased the nonhydrolytic closing rate of K1250A CFTR by approximately threefold (Fig. 6 E), just as it did at −120 mV

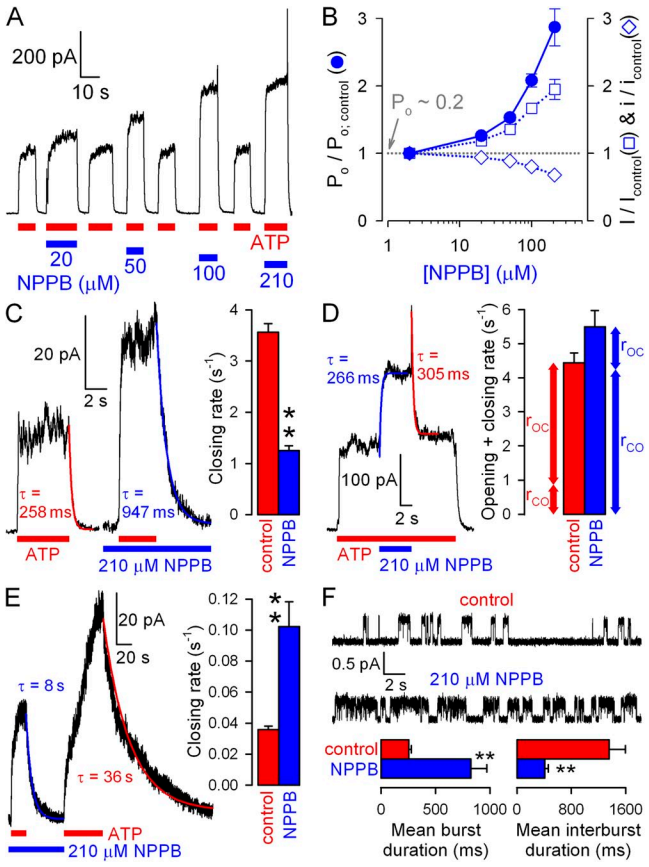

Figure 6. Gating stimulation by NPPB is largely voltage independent. (A) Dose-dependent stimulation by NPPB of steady-state macroscopic WT CFTR currents in 2 mM ATP at +60 mV. (B) Dose–response curves for fractional effects of NPPB on steady-state macroscopic current I (open squares; obtained from A), on unitary current i (open diamonds; obtained as in Fig. 1I), and on P_o (closed circles; obtained as in Fig. 2 E). (C; left) Macroscopic WT CFTR current at +60 mV elicited by brief exposures to 2 mM ATP in the absence or presence of 210 µM NPPB; colored lines, single-exponential fits (τ, time constants). (Right) Macroscopic WT closing rates (bars, $1/\tau$) in the absence (red) and presence of NPPB (blue). (D; left) Macroscopic WT CFTR current in 2 mM ATP at +60 mV and brief exposure to 210 µM NPPB; colored lines, single-exponential fits (τ, time constants). (Right) Sums of opening and closing rates (bars, $1/\tau$) in the absence and presence of NPPB; opening rates (r_{CO}, bottom vertical arrows) are estimated by subtraction of closing rates (r_{OC}, top vertical arrows) from the sums. (E; left) Macroscopic K1250A CFTR current at +60 mV elicited by exposures to 10 mM ATP in the absence or presence of 210 µM NPPB; colored lines, single-exponential fits (τ, time constants). (Right) Macroscopic K1250A closing rates (bars, $1/\tau$) in the absence (red) and presence (blue) of NPPB. (F; top) Currents from a single WT CFTR channel gating at +60 mV in 2 mM ATP before (top trace) and during (bottom trace) exposure to 210 µM NPPB; bandwidth, 100 Hz. (Bottom) Mean burst (left) and interburst (right) durations (bars) of WT CFTR in 2 mM ATP (red) and 2 mM ATP plus 210 µM NPPB (blue) at +60 mV. Bars were generated from 16 segments of record in ATP and 15 segments in ATP plus NPPB originating from nine patches; error bars represent SEM.

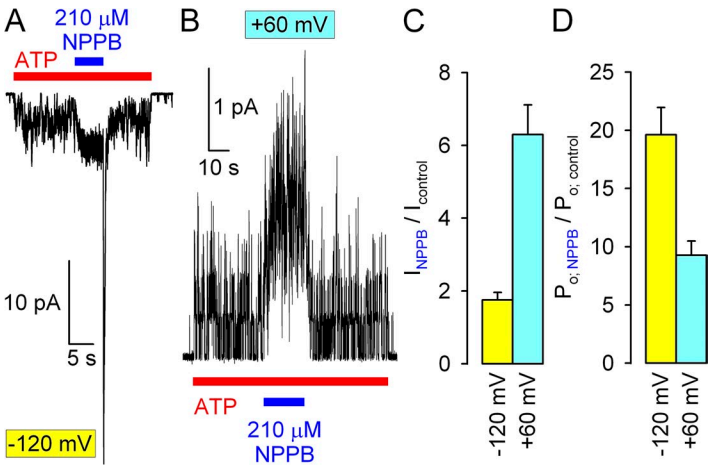

Figure 7. Stimulation of ΔF508 CFTR gating by NPPB. (A and B) Quasi-macroscopic currents of low temperature–rescued, prephosphorylated ΔF508 CFTR channels in 2 mM ATP at −120 mV (A) and +60 mV (B), and brief exposures to 210 μM NPPB. Note overall current stimulation by NPPB, and extreme current overshoot upon its removal, at −120 mV. (C and D) Fractional effects of 210 μM NPPB on (C) steady-state macroscopic currents and (D) P_o of ΔF508 CFTR at −120 mV (yellow bars) and +60 mV (cyan bars).

(Fig. 4, A and B). Because at +60 mV unitary currents remained resolvable even in the presence of 210 μM NPPB (Fig. 6 F), the conclusions drawn from nonstationary macroscopic analysis regarding effects on WT CFTR gating (Fig. 6, C and D) could be corroborated in steady-state single-channel recordings: as expected, 210 μM NPPB prolonged mean burst duration but shortened mean interburst duration, both by approximately threefold (Fig. 6 F, blue bars).

Stimulation of P_o by NPPB is enhanced for poorly active ΔF508 or unphosphorylated WT CFTR channels

In contrast to the three- to fourfold stimulation by NPPB of P_o for WT CFTR observed here, Wang et al. (2005) reported 10–15-fold stimulation of ΔF508 CFTR by NPPB. Indeed, we found that gating stimulation of low temperature–rescued ΔF508 CFTR by 210 μM NPPB is so robust that it overrides the pore block effect at all voltages, yielding overall current stimulation even at −120 mV (Fig. 7, A and C, yellow bar), and greater than fivefold stimulation at +60 mV (Fig. 7, B and C, cyan bar). Accounting for the pore block effect, these results suggest ∼20- and ∼8-fold stimulation of P_o at −120 and +60 mV, respectively (Fig. 7 D).

Interestingly, Wang et al. (2005) also reported a dependence of NPPB stimulation on the phosphorylation state of WT CFTR. Whereas all the data in Figs. 2–6 were obtained in the relatively stable, partially dephosphorylated state of CFTR, after removal of PKA (Csanády et al., 2010), we indeed observed an ∼10-fold stimulation of the small current, carried by low P_o activity of unphosphorylated WT CFTR channels, when 210 μM NPPB was applied at +60 mV before exposure of the patch to PKA (Fig. 8, A, first application of NPPB [expanded in inset], and B, left). In contrast, in the same patch, 210 μM NPPB had little effect on overall current at +60 mV when applied in the presence of PKA, i.e., to fully phosphorylated channels that are gating at high P_o (Fig. 8, A, second application of NPPB, and B, right), whereas soon after PKA removal, it increased by approximately twofold the current carried by partially dephosphorylated channels, which are gating at intermediate

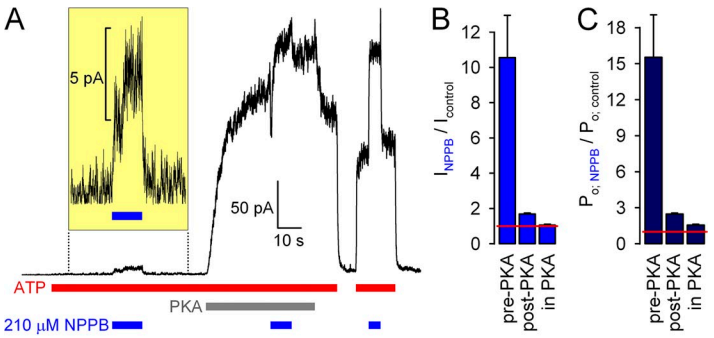

D

Condition	control τ_b	control τ_{ib}	control P_o	210 μM NPPB τ_b	210 μM NPPB τ_{ib}	210 μM NPPB P_o	Stimulation
pre-PKA	250 ms	80 s	0.003	1 s	20 s	0.048	15x
in PKA	750 ms	1 s	0.43	3 s	250 ms	0.92	2x
post-PKA	250 ms	1 s	0.2	1 s	250 ms	0.8	4x

Figure 8. Phosphorylation dependence of NPPB stimulation of WT CFTR reflects nonlinear dependence of P_o on opening and closing rates. (A) Macroscopic WT CFTR currents in 2 mM ATP at +60 mV, and applications of 210 μM NPPB before exposure to (current scale magnified in inset), in the presence of, and after removal of 300 nM PKA catalytic subunit. (B and C) Fractional effects of 210 μM NPPB on (B) steady-state macroscopic currents and (C) P_o of unphosphorylated (pre-PKA), fully phosphorylated (in PKA), and partially dephosphorylated (post-PKA) WT CFTR channels at +60 mV. (D) Table summarizing expected changes in gating parameters assuming a constant (phosphorylation-independent) fourfold increase in τ_b and fourfold decrease in τ_{ib} in the presence of 210 μM NPPB, as measured in this study for the post-PKA condition at −120 mV (Fig. 3; slightly smaller, approximately threefold, effects were measured at +60 mV; Fig. 6). Control parameters (left column) reflect typical values measured for WT CFTR in this and previous studies (e.g., Csanády et al., 2005; Szollosi et al., 2010); the post-PKA values in NPPB (right column, bottom row) reflect the values measured in Fig. 3.

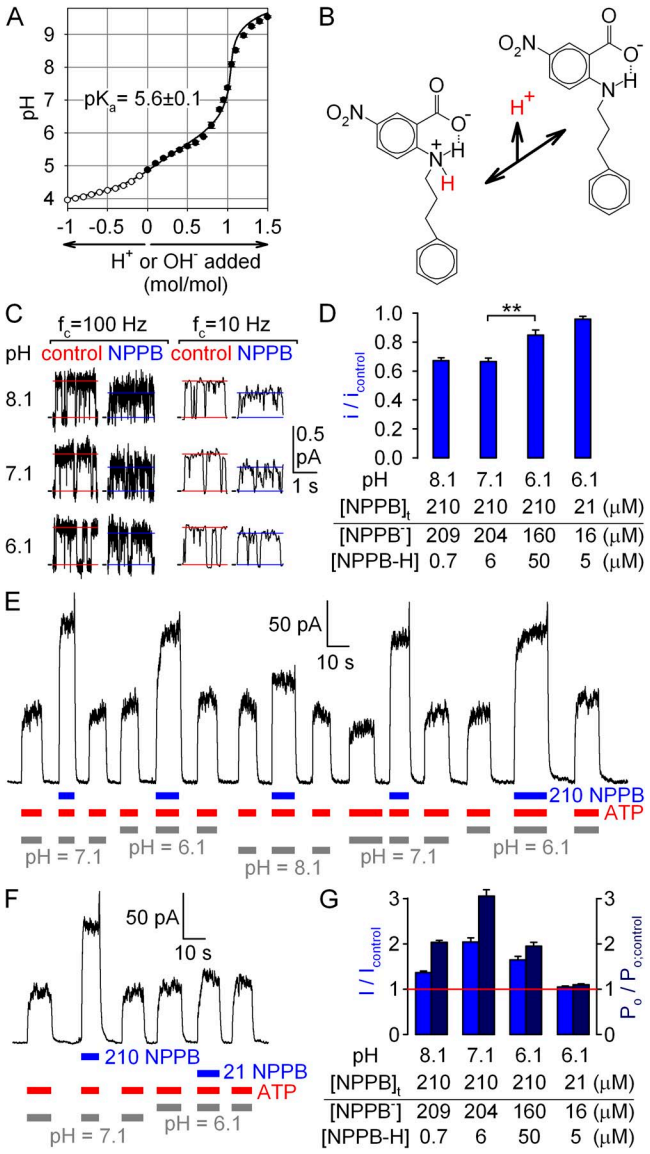

Figure 9. Anionic form of NPPB is responsible for the observed gating effects. (A) Titration curve of NPPB; 10 ml 100 μM NPPB (in H_2O) was titrated with 10-μl aliquots of either 10 mM NaOH (closed symbols; $n = 3$) or 10 mM HCl (open symbols; $n = 2$, plotted on negative side of abscissa). Solid line is a fit to the titration curve of a monoprotic weak acid, corrected for the presence of 10 mM CO_2 (see Materials and methods); fitted pK_a is plotted. (B) Structures of protonated (zwitterionic) and deprotonated (anionic) forms of NPPB; the proton released with a pK_a of ∼5.6 is highlighted in red; dotted line depicts suggested hydrogen bond. (C) Segments of unitary current at +60 mV from a single locked-open E1371S CFTR channel in symmetrical ∼140-mM Cl^- at three different cytosolic pH values, with and without cytosolically applied 210 μM NPPB, displayed at two bandwidths (f_c, filter corner frequency). Horizontal lines depict closed current level and average current through a bursting channel. (D) Apparent unitary amplitudes (of heavily filtered currents), normalized to those obtained in the absence of NPPB at the respective pH (bars). Table lists concentrations of anionic and uncharged NPPB for the tested conditions, calculated using a pK_a of 5.6. (E and F) Stimulation at +60 mV of steady-state macroscopic WT CFTR currents in 2 mM ATP (red bars) by the application of (E and F) 210 μM NPPB (blue bars) at bath pH values of 6.1, 7.1, and 8.1 (gray bars), or of (F) 21 μM NPPB at a bath pH value of 6.1. (G) pH dependence of fractional effects of NPPB on steady-state macroscopic current I (blue bars; obtained from E and F), and on P_o (dark blue bars; $P_o/P_{o;\,control}$ was calculated as the ratio $(I/I_{control}):(i/i_{control})$). (Table) Concentrations of anionic and uncharged NPPB for the tested conditions, assuming pK_a = 5.6.

P_o (Fig. 8, A, last NPPB application, and B, middle). Accounting for the pore block, these effects of NPPB on overall WT CFTR current at +60 mV correspond to ∼15-, ∼3-, and <2-fold stimulation of P_o of poorly, partially, and fully phosphorylated CFTR (Fig. 8 C). These data confirm the findings of Wang et al. (2005) and suggest that NPPB stimulates P_o much more efficiently when the starting P_o value is low.

Anionic form of NPPB is responsible for the observed gating stimulation

At our bath pH of 7.1, the anionic, deprotonated form of NPPB dominates, and only a small fraction of the compound is protonated, uncharged. Although the pore block is no doubt attributable to the anionic form of NPPB ($NPPB^-$), we wanted to identify whether it is this anionic form or perhaps the less prevalent protonated form (NPPB-H) that is responsible for gating stimulation.

Because we found no reliable data in the literature for the pK_a value of NPPB (most studies assumed a pK_a of ∼4.5 by referring either to the study of Wangemann et al., 1986, in which the pK_a was not measured, or to that of Walsh and Wang, 1998, in which no data were shown), we determined the latter by electrometric titration. Because of the limited solubility of NPPB in water (especially at low pH), titration by NaOH (Fig. 9 A, closed circles) and HCl (Fig. 9 A, open circles) could be performed only for a dilute (100-μM) aqueous solution of the compound, restricting reliable determination of potential pK_a values to the range of 4–10. (At this low concentration, a weak acid with a pK_a of <4 is largely dissociated, whereas a site with a pK_a of >10 remains largely protonated even after the addition of 1 mol/mol NaOH.) The data were well fit (Fig. 1 A, solid line) by a titration curve expected for a monoprotic weak acid and revealed a single pK_a value of ∼5.6 in the range of 4–10.

To deconvolve gating and permeation effects of NPPB at various pH, we first characterized pore block at +60 mV by 210 μM of total [NPPB] applied at bath pH values of 8.1, 7.1, and 6.1 (Fig. 9 C). Whereas average unitary currents, determined from heavily filtered current traces, decreased to ∼67% of control when 210 μM NPPB was applied at pH 7.1 or 8.1 (Fig. 9 D, left; compare to Fig. 1 D), at pH 6.1 the pore block was significantly ($P = 8 \times 10^{-4}$) milder, yielding a fractional decrease in unitary current of only ∼15% (Fig. 9 D, third bar). This is consistent with a significantly decreased concentration of $NPPB^-$ at this low pH, as

predicted by the measured pK_a value of 5.6 (see table in Fig. 9 D).

We next assayed macroscopic current stimulation at +60 mV by 210 µM of total NPPB at various pH (Fig. 9 E). Fractional current stimulation at pH 6.1 was not enhanced relative to that measured at our control pH of 7.1 (Fig. 9 E and middle blue bars in G), despite an ∼10-fold higher concentration of uncharged NPPB-H at the lower pH (Fig. 9 G, table); in fact, the calculated effect on P_o was significantly blunted at pH 6.1 (Fig. 9 G, middle dark blue bars). Furthermore, no significant stimulation of P_o was observed when applying 21 µM of total NPPB at pH 6.1 (Fig. 9 F and right side of G), a condition in which [$NPPB^-$] is selectively lowered, whereas [NPPB-H] remains comparable to that calculated for 210 µM of total NPPB at pH 7.1 (Fig. 9 G, table). These results rule out uncharged NPPB-H as the active form responsible for gating stimulation and suggest that the latter is largely caused by anionic $NPPB^-$.

In principle, the reduced fractional stimulation of P_o by 210 µM of total NPPB at pH 6.1 could be taken as an indication that uncharged NPPB-H is entirely inactive; however, we refrain ourselves from such a conclusion, as fractional current stimulation was also blunted at pH 8.1 (Fig. 9 E and left blue bar in G) relative to pH 7.1, despite slightly higher $NPPB^-$ at the higher pH (Fig. 9 G, table). The similarly reduced fractional effect on P_o at both pH 6.1 and 8.1 (Fig. 9 G, compare first and third dark blue bars) suggests that changes in surface properties and/or gating kinetics of the CFTR protein at both acidic and basic pH should also be considered (compare to Chen et al., 2009).

DISCUSSION

Until very recently, treatment of CF has been exclusively symptomatic. This has changed with the approval of VX-770 (ivacaftor; Vertex Pharmaceuticals; Van Goor et al., 2009; Ramsey et al., 2011), the first drug shown to act by binding specifically to the CFTR protein. However, to date it has been shown to benefit only patients carrying at least one G551D allele, which constitute <5% of the CF population. Effective drug therapy to treat patients carrying ΔF508 alleles is still lacking. At present, there is a wide gap between industrial efforts to obtain drugs targeting CFTR and academic research aimed at understanding CFTR structure and mechanism at a molecular level. Although industrial high-throughput screening has clearly met some success (Van Goor et al., 2009; Ramsey et al., 2011), the wealth of information that has emerged from basic research has yet to impact drug discovery. In this study, we have identified two strategic points in CFTR's unique functional cycle that are eminently suited as intervention points for altering CFTR activity: the channel opening step, and the step that rate limits channel closure (hydrolytic $O_1 \rightarrow O_2$ step). Our dissection of the mechanism of action of NPPB, presented here, shows how affecting these transitions can powerfully influence P_o of WT and mutant (including ΔF508) CFTR channels, and offers a route to rational design of drugs targeting CFTR.

Our interpretation builds on the nonequilibrium nature of the CFTR gating cycle (see the simplified cyclic gating model depicted throughout the insets of Figs. 3–5), which is rooted in its evolutionary descent from an ancestral ABC transporter. First proposed by Vergani et al. (2003), this model was later tested and refined (Vergani et al., 2005; Csanády et al., 2006, 2010; Bompadre et al., 2007; Tsai et al., 2010) before becoming generally accepted (Gadsby et al., 2006; Chen and Hwang, 2008; Hwang and Sheppard, 2009; but compare to Aleksandrov et al., 2009). Recently, various extensions of this scheme have been suggested to explain the rare openings (P_o of ∼0.004), in the absence of ATP, of unliganded WT (Szollosi et al., 2010) or G551D CFTR (Bompadre et al., 2007), enhancement of such activity by cytosolic loop mutations (Wang et al., 2010), and [ATP]-dependent prolongation of open burst durations in mutants (Jih et al., 2012b) or by drugs (Jih and Hwang, 2013). Although these extended models differ in detail (Szollosi et al., 2010; Kirk and Wang, 2011; Jih et al., 2012a), they all contain, as a common core, the basic cycle depicted in our figure insets, which describes the majority of gating events for both WT CFTR and many CFTR mutants, including ΔF508 (Jih et al., 2011; but compare to Wang et al., 2005, for ATP-independent G551D). We will therefore use the core cyclic model as a framework for discussing our results.

Voltage-dependent pore block and gating stimulation are distinct NPPB effects

Our study clearly distinguishes the effects of NPPB on gating from its voltage-dependent pore-blocker effects. Although stimulation by NPPB was originally only noted at positive potentials (Wang et al., 2005), careful comparison of effects on unitary versus macroscopic currents demonstrates robust stimulation of P_o even at −120 mV (Fig. 2). In fact, because of its dual action on both i and P_o, fractional reduction of macroscopic current by NPPB is not a good measure of pore block, unless observed on "locked-open" channels, which are not gating (P_o of ∼1), such as surviving E1371S (Fig. 1, E and I) or K1250A (Fig. 4 D, inset) channels after the removal of ATP. This might explain previously reported lower values (−0.35, Zhang et al., 2000; −0.2, Zhou et al., 2010) for the effective valence of the NPPB block than found here (approximately −0.5; Fig. 1, D–F). Of note, Ai et al. (2004) found an effective valence of approximately −0.5 for CFTR pore block by anthracene-9-carboxylate (9-AC), a compound that also stimulates P_o of CFTR, suggesting that NPPB, MOPS, and 9-AC likely share a common binding site in the pore; possibly, gating

stimulation by NPPB and 9-AC might also involve a shared binding site.

We show here that all gating effects of NPPB are indeed largely voltage independent at a microscopic level (Fig. 6, A–F; except for slightly smaller effects at +60 mV), as expected if gating and pore block effects involve distinct binding sites. Accordingly, although the apparent K_I of NPPB for pore block was ∼20 µM at −120 mV (Fig. 1 J; replotted in Fig. 10, open diamonds), the apparent $K_{1/2}$ for slowing hydrolytic closure of WT CFTR (Fig. 10, closed circles) was at least four times higher (∼90 µM), and a tentative fit to the dose–response curve for acceleration of nonhydrolytic closure (measured for the K1250A mutant; Fig. 10, closed squares) suggested a similar $K_{1/2}$ of ∼100 µM (although reliability of the latter fit is limited by the uncertainty of its asymptotic value). Consistent with our interpretation of distinct binding sites for pore block and gating effects, replacement of the negatively charged carboxyl moiety of NPPB by an uncharged amide group eliminated pore block and yielded a pure potentiator compound, which stimulated gating of both WT and ΔF508 CFTR at all voltages (Wang et al., 2005).

Anionic form of NPPB stimulates gating

Although the uncharged amide analogue of NPPB stimulates CFTR (Wang et al., 2005), the gating effect of NPPB was not enhanced at acidic pH, ruling out uncharged, protonated NPPB-H, which is present at low micromolar concentrations at our standard bath pH of 7.1, as the cause of the observed gating stimulation. We therefore conclude that the stimulatory effect observed in this study is largely caused by anionic $NPPB^-$. Of note, NPPB-H is not expected to be a good mimic of the amide analogue. This is because the single pK_a value of ∼5.6, which we could detect in the range of pH 4–10 (Fig. 9 A), is unlikely to reflect titration of the carboxylate group, but rather that of the secondary amino group of NPPB (Fig. 9 B). Indeed, in 3-nitrobenzoic acid, the pK_a of the carboxylate is ∼3.5, and for 2-aminobenzoic acid, the two pK_a values are ∼2.1 (for the carboxylate) and ∼5.0 (for the amino group). (Referenced pK_a values were taken from a table available at http://www.zirchrom.com/organic.htm.) The unusually low pK_a for the amino group in the latter compound is caused by the electron-withdrawing effect of the aromatic ring (compare, pK_a is ∼4.7 for aniline and ∼5.1 for the secondary amino group of *N*-ethyl aniline), whereas the unusually low pK_a of its carboxylate group is partly caused by a hydrogen bond between the adjacent amino group (donor) and a carboxylate oxygen (acceptor); such a hydrogen bond is likely to form also in NPPB (Fig. 9 B, dotted line). Thus, we interpret the measured pK_a value of ∼5.6 for NPPB to reflect that of the amino group, whereas that of the carboxylate must be too low (<3) to be detected in a dilute (100-µM) solution. This assignment predicts that NPPB-H, the uncharged form of NPPB that accumulates at pH 6.1 (Fig. 9 G, table), is in fact a zwitterion, unlike its amide analogue.

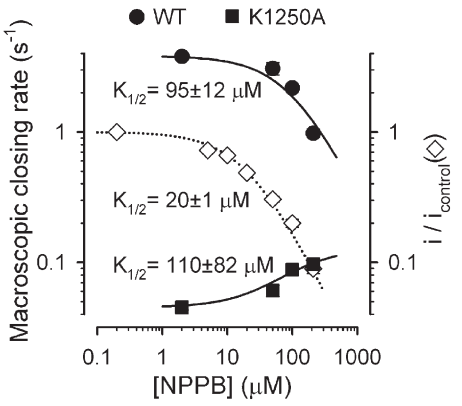

Figure 10. Dose dependence of NPPB gating effects. Macroscopic closing rates of WT (closed circles) and K1250A (closed squares) CFTR in the presence of various cytosolic [NPPB], measured at −120 mV using the protocols shown in Figs. 3 A and 4 A, respectively; leftmost data points represent control values in the absence of NPPB. The 50- and 100-µM data points for K1250A were measured at −40 mV. Solid lines are fits to the equation $r_{OC}([NPPB]) = r_0 + (r_\infty - r_0)([NPPB]/([NPPB] + K_{1/2}))$, with r_∞ fixed to zero for WT but left free for K1250A; $K_{1/2}$ values are plotted. Open diamonds and dotted line depict fractional pore block at −120 mV, replotted from Fig. 1 J.

One explanation for the smaller stimulation of P_o by NPPB at low pH would be if zwitterionic NPPB-H did not act as a stimulator at all. However, because the efficiency of gating stimulation declined both at acidic and basic pH (Fig. 9 G, dark blue bars), it is likely that changes in the surface charge distribution of the CFTR protein, as well as its gating kinetics, are at least partly responsible for the decreased responses at extreme pH. Indeed, in experiments performed at 37°C, Chen et al. (2009) found that P_o of WT CFTR decreases monotonically with increasing pH, within the range of 6.3–8.3. The approximately twofold higher P_o at pH 6.3 compared with 8.3 was largely caused by approximately three- to fourfold longer mean open burst durations at the lower pH. Although at 25°C steady-state values of macroscopic currents appeared less sensitive to pH (Fig. 9 E), current relaxation rates upon the addition of ATP, which reflect the sum of the opening and closing rate, were indeed visibly slower at pH 6.1, but faster at pH 8.1, when compared with those observed at pH 7.1 (compare to Fig. 9 E), reporting profoundly altered gating kinetics at both extreme values of pH. In addition to the above instantaneous effects of pH on gating kinetics, we also typically observed a progressive decline in macroscopic CFTR currents upon prolonged exposure to pH 8.1 (see Fig. 9 E), suggesting that the CFTR protein is either dephosphorylated more rapidly, or otherwise progressively inactivates at very high pH. These

limitations impede us from concluding whether zwitterionic NPPB-H can act as a gating stimulator or not.

NPPB catalyzes channel opening

NPPB stimulates P_o by two distinct mechanisms: one increasing opening (and nonhydrolytic closing) rate, the other slowing the microscopic rate of hydrolysis ($O_1 \rightarrow O_2$ transition). The first action is a stabilization by ~1 *k*T of the $C_1 \leftrightarrow O_1$ transition state, a bona fide catalyst effect, which results in comparable (approximately threefold) acceleration of "forward" channel opening rate (Figs. 3 F and 6, D and F) and "backward" nonhydrolytic closing rate (Figs. 4 B and 6 E). At first glance, it might seem surprising that a catalyst should enhance the P_o of an ion channel. Indeed, for an equilibrium mechanism (Fig. 11 A, left, red rates), a catalyst, by lowering the free-energy barrier $\Delta G^{\ddagger}$ (Fig. 11 B, left, blue vs. red ΔG profile), simultaneously speeds both the opening and closing rate by the same factor (Fig. 11 A, left, blue rates), causing no change in P_o (Fig. 11 C, left). Accordingly, for the nonhydrolytic K1250A mutant, which gates at equilibrium, NPPB speeds gating transitions but does not alter P_o (Fig. 4 E). In contrast, WT CFTR, because of its unique nonequilibrium cycle, enters and exits the open state through different pathways, rate-limited by the $C_1 \rightarrow O_1$ and the $O_1 \rightarrow O_2$ transitions, respectively; the rates of these transitions are determined by the height of the corresponding energetic barriers ($\Delta G^{\ddagger}_{C1 \rightarrow O1}$ and $\Delta G^{\ddagger}_{O1 \rightarrow O2}$; Fig. 11 B, right, red ΔG profile). Thus, for WT CFTR, lowering the $C_1 \leftrightarrow O_1$ barrier (Fig. 11 B, right, blue ΔG profile) selectively speeds the opening rate, without speeding the closing rate (as long as $\Delta G^{\ddagger}_{O1 \rightarrow C1}$ remains substantially larger than $\Delta G^{\ddagger}_{O1 \rightarrow O2}$). For transition rates typical to WT CFTR under our recording conditions (Fig. 11 A, right, red rates), this catalyst effect alone of NPPB (Fig. 11 A, right, blue rates) provides an approximate two- to threefold stimulation of P_o (Fig. 11 C, right).

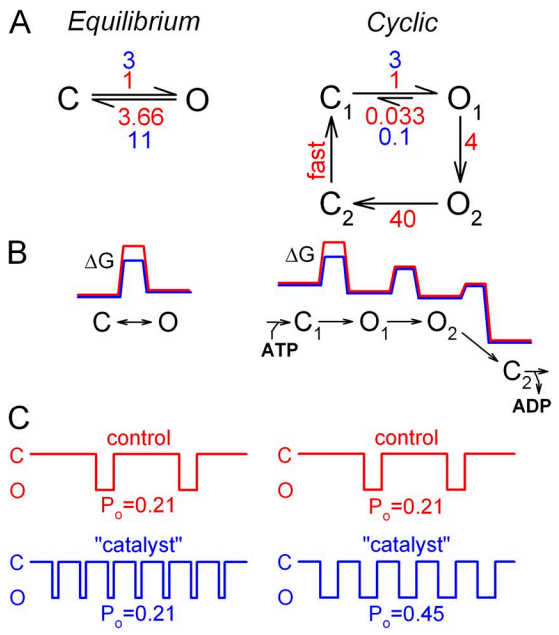

Figure 11. Catalyst effect as a unique strategy to enhance P_o of a nonequilibrium ion channel. (A) Simple equilibrium scheme (left) and cyclic nonequilibrium scheme (right; compare to cartoons in Figs. 3–5), with transition rates in the absence (red) and presence (blue) of a catalyst for step C↔O (left) or $C_1 \leftrightarrow O_1$ (right). (B) Free energy profiles (not drawn to scale) for the schemes in A, in the absence (red) and presence (blue) of the same catalyst. (C) Illustration of channel gating patterns, and calculated P_o, for the schemes in A, in the absence (red) and presence (blue) of the catalyst.

Thermodynamic studies have provided some insight into the nature of the opening transition state, outlining it as a high enthalpy structure in which the NBD dimer has already formed, but the pore is still closed, causing molecular strain at the TMD–NBD interface (Csanády et al., 2006; Wang et al., 2010). Recent ABC transporter crystals revealed the 3-D structure of this interface and how it changes in different functional states (Dawson and Locher, 2006; Hohl et al., 2012). For CFTR, a homology model, thought to represent a channel open state, predicted physical interactions between phenylalanine 508 on the NBD1 surface and a cluster of aromatic residues in the fourth intracellular TMD loop (Serohijos et al., 2008). However, in a structure thought to represent the closed CFTR state, the fourth intracellular loop is not in proximity of the residue corresponding to F508 (Hohl et al., 2012). A loss of stabilizing interactions present in the opening transition state, but not in the closed ground state, could explain why the major gating defect caused by disease mutation ΔF508 is an increase in $\Delta G^{\ddagger}_{C1 \rightarrow O1}$, reflected by a dramatic (~30-fold; Miki et al., 2010) reduction in channel opening rate, and why P_o of this mutant is robustly stimulated by NPPB (Wang et al., 2005).

NPPB slows channel closing by inhibiting the hydrolysis step

The second effect of NPPB on WT CFTR gating was an approximately fourfold slowing of channel closing rate (Figs. 3, A and C, and 6, C and F). Using maximum likelihood fitting of burst duration distributions, we show that NPPB delays closure by slowing the $O_1 \rightarrow O_2$ transition (Fig. 5, C–E). Thus, NPPB bound at its "gating site" slows ATP hydrolysis at site 2 of the NBD dimer interface. This allosteric action implies a significant conformational change at that NPPB binding site upon ATP hydrolysis at site 2, consistent with the proposal by Gunderson and Kopito (1995) of a TMD conformational change associated with this step. Because the (likely very slow) rate of reversal of the $O_1 \rightarrow O_2$ step cannot be measured (Csanády et al., 2010), we cannot tell whether NPPB causes an isolated destabilization of the $O_1 \rightarrow O_2$ transition state (a pure "anticatalyst" effect), or whether the stability of the O_2 ground state also changes relative to O_1.

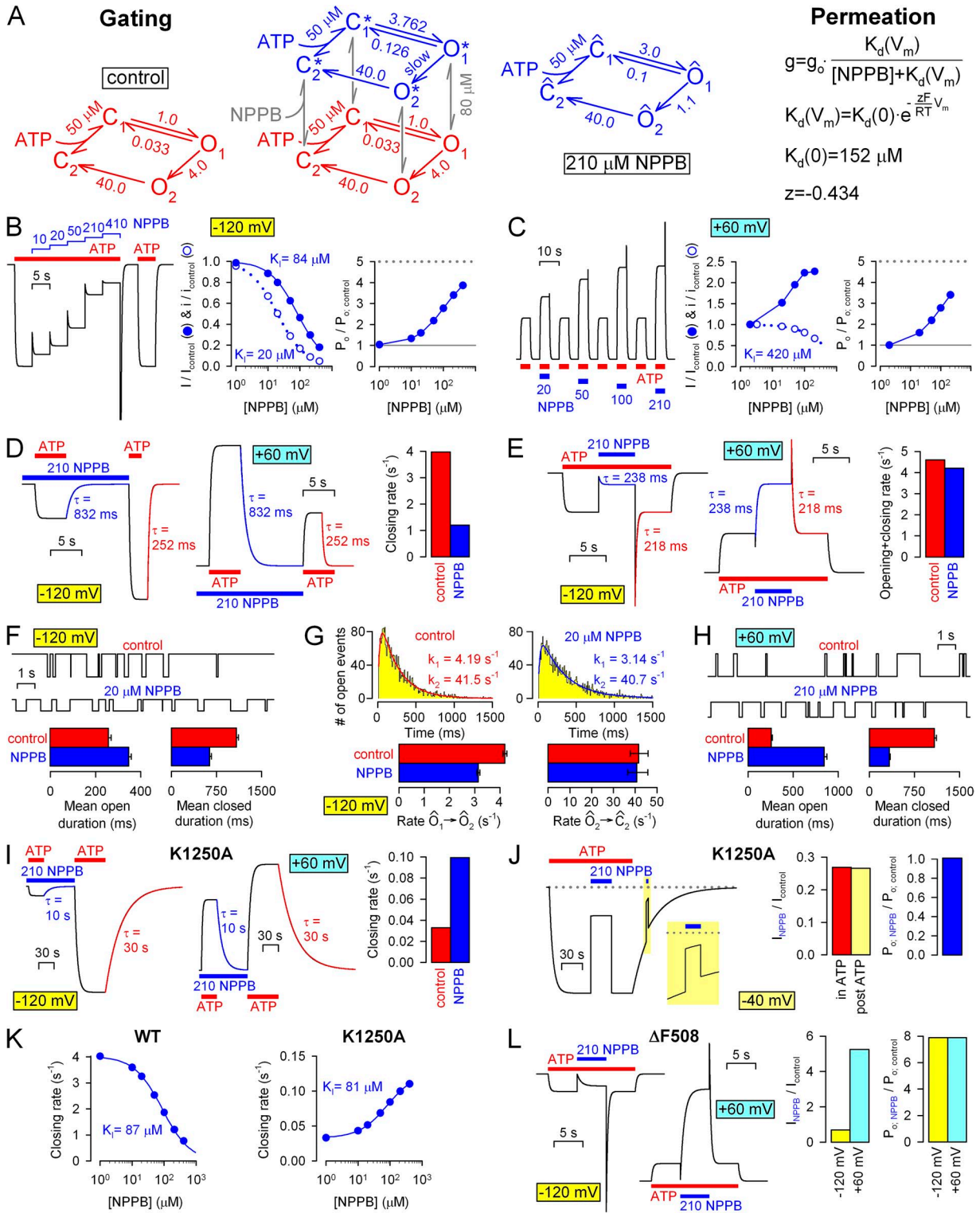

Figure 12. Full kinetic model of NPPB effects on CFTR gating and permeation. (A; left) Two-tiered kinetic model of NPPB gating effects (cube). States C_1, O_1, O_2, and C_2 (red) correspond to the four states depicted in the cartoons in Figs. 3–5 and represent states in which NPPB is not bound at its "gating site." The $C_2 \leftrightarrow C_1$ transition, which reflects exchange of ADP for ATP at site 2, is modeled as a single step, with a K_d of 50 μM for ATP. For simplicity, a single voltage-independent K_d of 80 μM is used to characterize rapid binding/unbinding of NPPB to the gating site in all four conformational states (vertical transitions; gray arrows). States C_1*, O_1*, O_2*, and C_2* (blue) are conformational states analogous to C_1, O_1, O_2, and C_2, but with NPPB bound at the gating site. In 0 or 210 μM NPPB, the full model (cube) reduces to the four-state models to its left (red) and right (blue), respectively; states $\hat{X}$ in the blue reduced model are compound states ($\hat{C}_1 = \{C_1; C_1^*\}$, $\hat{O}_1 = \{O_1; O_1^*\}$, etc.), and printed rates are apparent rates of transition between them. (Right) Voltage

Prolongation of bursts by NPPB was already noted by Zhang et al. (2000) and interpreted as a "foot-in-the-door" mechanism: the presence of the blocker physically preventing gate closure. Several of our observations are inconsistent with such an assignment. First, unlike the pore block, the effect on burst duration shows little voltage dependence (compare Figs. 3 C and 6 C). Second, a foot-in-the-door mechanism would be expected to slow the actual closing step, transition $O_2 \rightarrow C_2$, for which we find no evidence (Fig. 5 E). Third, the presence of NPPB does not slow closure of the nonhydrolytic mutant K1250A (Fig. 4, A and B), confirming that the gate can close with NPPB bound in the pore, just as it can close in the presence of bound $MOPS^-$, as the latter does not affect the closing rate of either WT (Fig. 3, B and C) or K1250A CFTR (Fig. 4, A and B). Note that the similar effective valences of NPPB and $MOPS^-$ (Fig. 1, D, F, and H) suggest that their blocking sites are close to each other. The fact that the gate can close with either blocker bound is consistent with an extracellularly localized gate (Bai et al., 2011; Norimatsu et al., 2012), as predicted by the ABC transporter analogy, based on which CFTR's closed-pore conformation corresponds to inward-facing TMDs. Collectively, these results rule out a classical open-channel block mechanism as an explanation for the delayed pore closure in NPPB. Moreover, the differential effect of NPPB on hydrolytic versus nonhydrolytic closing rate (compare Figs. 3 C and 4 B) adds further support for an underlying nonequilibrium gating cycle.

The potentiator compound Vx-770, now approved for the treatment of CF patients carrying the G551D mutation, was proposed to slow closure of WT CFTR by facilitating a reentry pathway from state O_2 to state O_1, which would allow ADP in site 2 to be replaced by a new ATP molecule without intervening pore closure (Jih and Hwang, 2013). Such a mechanism would prolong steady-state burst durations by allowing occlusion and hydrolysis of more than one ATP molecule in site 2 within a single burst. In contrast, the macroscopic relaxation time constant after ATP removal measures mean burst duration in the absence of bath ATP, i.e., without the possibility of ATP rebinding. Because the macroscopic closing time constant in the presence of 210 µM NPPB (Fig. 6 C, blue time constant; $\tau_{relaxation} = 847 \pm 60$ ms; $n = 14$) is indistinguishable from the steady-state mean burst duration (Fig. 6 F; $\tau_{burst} = 825 \pm 145$ ms; $n = 15$), we conclude that NPPB prolongs open bursts without significantly changing the near 1:1 coupling between ATP occlusion events and channel bursts of WT CFTR.

Proposed NPPB mechanism of action can account for very potent stimulation of ΔF508 CFTR

Our kinetic analysis accounts for the three- to fourfold stimulation by NPPB of P_o for WT CFTR, but does it account for the 10–15-fold stimulation of ΔF508 CFTR reported by Wang et al. (2005)—also reproduced here (Fig. 7)—which makes NPPB the most potent drug targeting this disease mutant available to date? Because P_o is a nonlinear function of mean burst and interburst durations ($P_o = \tau_b/(\tau_b + \tau_{ib})$), such discrepancies between overall stimulation efficiencies and effects on microscopic rates are actually expected. Whenever the "control" (without NPPB) value of P_o is low ($\tau_b << \tau_{ib}$), the approximately fourfold increase in τ_b (Fig. 3 A; approximately threefold at +60 mV; Fig. 6 F) and approximately fourfold decrease in τ_{ib} (Fig. 3 F; approximately threefold at +60 mV; Fig. 6 F) should affect P_o independently, predicting an ∼16-fold stimulation (approximately ninefold at +60 mV), in very good agreement with our observations on ΔF508 CFTR (Fig. 7). This same argument also explains the observed dependence of stimulatory efficiency on phosphorylation level (Fig. 8 C; compare to Wang et al., 2005). Indeed, assuming a constant (entirely phosphorylation-independent) fourfold effect of 210 µM NPPB on both τ_b and τ_{ib} predicts ∼15-, ∼2-, and ∼4-fold effects on P_o for unphosphorylated (before exposure to PKA, P_o of ∼0.003), fully phosphorylated (in the presence of PKA, P_o of ∼0.4), and partially dephosphorylated (after PKA removal, P_o of ∼0.2) WT CFTR (see table in Fig. 8 D), in good agreement with our experiments (Fig. 8, A–C). Note that at +60 mV, the approximately twofold increase in P_o of fully phosphorylated channels is largely counteracted by pore block, yielding little net effect (Fig. 8 B; compare to Wang et al., 2005).

Simple unified kinetic model captures most key features of observed NPPB effects

Our conclusions on the gating effects of NPPB can be summarized in a simple model that treats gating and

and dose dependence of pore block by NPPB is modeled as an instantaneous effect on apparent unitary conductance (g) and is approximated by the Boltzmann equation with parameters printed (g_0, control unitary conductance; T, temperature in Kelvin; $R = 8.31$ J · mol^{-1} · K^{-1}; F = 96,500 C · mol^{-1}). (B–L) Predictions of the model in A for the experimental protocols and analysis results obtained in this study. Macroscopic current time courses for the experimental protocols in B–E and I–L were calculated, whereas single-channel traces for F–H were simulated using standard Q-matrix techniques (Colquhoun and Sigworth, 1995). Rate $O_1^* \rightarrow O_2^*$ was tentatively set to zero. Gating effects of the K1250A mutation were modeled by setting rate $O_1 \rightarrow O_2$ to zero while increasing the K_d for ATP to 5 mM (Vergani et al., 2003), those of the ΔF508 mutation were modeled by decreasing rate $C_1 \rightarrow O_1$ 30-fold while increasing rate $O_1 \rightarrow C_1$ threefold (Miki et al., 2010; Jih et al., 2011). Analysis of macroscopic currents was done as described in Figs. 2–4, 6, 7, and 10. For F and H, five independent events lists, containing 100 open events each, were simulated for each condition; bar charts show mean ± SEM of obtained mean open and closed times. Open duration histograms in G were created from 3,000 simulated open events for both conditions and fitted by maximum likelihood as described for Fig. 5 (C–E).

permeation effects separately (Fig. 12 A, left and right).

Gating (Fig. 12 A, left) is described by a simple two-tiered mechanism (Fig. 12 A, cube), in which the bottom tier represents gating states with NPPB not bound at the gating site and is identical to the four-state model depicted throughout the cartoons in Figs. 3–5. The $C_2 \rightarrow C_1$ transition reflects the exchange of ADP for ATP at site 2, which in reality takes place in two sequential steps (ADP unbinding followed by ATP binding). Because under our recording conditions, in which the cytosolic face of the patch is continuously perfused with an ADP-free bath solution, unbinding of ADP is irreversible (and likely rapid), ADP–ATP exchange is modeled here as a single step, with a K_d for ATP of 50 μM (Csanády et al., 2000). Channel opening rate (rate $C_1 \rightarrow O_1$) represents the inverse of the observed mean interburst duration (~1 s for WT CFTR; Figs. 5 B and 6 F). Rates $O_1 \rightarrow O_2$ and $O_2 \rightarrow C_2$ reflect the fast and slow rate, respectively, obtained from fits to the distributions of open burst durations of WT CFTR (k_1 and k_2 in Fig. 5 C). Finally, rate $O_1 \rightarrow C_1$ represents the slow rate of nonhydrolytic closure, modeled by the closing rates of nonhydrolytic mutants K1250A (Fig. 4 A) or E1371S (Fig. 1 K), or of WT channels that have been locked open by ATP plus pyrophosphate (Fig. S2); the time constant of this slow process is ~30 s.

Vertical transitions (Fig. 12 A, gray arrows) reflect binding/unbinding of NPPB to the gating site. Although our data do not provide direct estimates of these rates, the onset of the gating effects both upon the addition and removal of NPPB appeared instantaneous (e.g., Figs. 3 D, 6 D, and 7, A and B), without observable delay (which would have caused relaxation time courses to become sigmoidal). This suggests that NPPB is at rapid equilibrium with the gating site, at least compared with the rate of our solution exchange, and hence relative to the rates of CFTR gating. For simplicity, we assumed a single voltage-independent K_d of 80 μM in all four conformational states.

States C_1*, O_1*, O_2*, and C_2* of the top tier (Fig. 12 A, blue) are conformational states analogous to C_1, O_1, O_2, and C_2, but with NPPB bound at the gating site. In the absence of NPPB, the full model (Fig. 12 A, cube) reduces to the four-state model to its left (red). Moreover, because of the rapid equilibrium of NPPB with its gating site, in the presence of NPPB, each state of the bottom tier is at rapid equilibrium with the analogous state of the top tier, so that each pair can be treated kinetically as a single compound state. Thus, even in the presence of NPPB, the full scheme readily reduces to a four-state model with compound states $\hat{C}_1 = \{C_1; C_1^*\}$, $\hat{O}_1 = \{O_1; O_1^*\}$, $\hat{O}_2 = \{O_2; O_2^*\}$, and $\hat{C}_2 = \{C_2; C_2^*\}$. Apparent transition rate $\hat{X}_i \rightarrow \hat{Y}_j$ is obtained as $p_i k_{ij} + p_i^* k_{ij}^*$, where $p_i = P\left(X_i \middle| \hat{X}_i\right)$, $p_i^* = P\left(X_i^* \middle| \hat{X}_i\right)$, k_{ij} is rate $X_i \rightarrow Y_j$, and k_{ij}^* is rate $X_i^* \rightarrow Y_j^*$; fractional occupancies p_i and p_i^* are given by $p_i = K_d/(K_d + [\text{NPPB}])$ and $p_i^* = [\text{NPPB}]/(K_d + [\text{NPPB}])$. In 210 μM NPPB, the full scheme (Fig. 12 A, cube) reduces to the four-state model to its right (blue): apparent rate $\hat{C}_1 \rightarrow \hat{O}_1$ reflects the observed opening rate in 210 μM NPPB (Figs. 3 F and 6, B and F), rate $\hat{O}_1 \rightarrow \hat{O}_2$ is the rate-limiting step for closure and reflects closing rate in 210 μM NPPB (Figs. 3 C and 6, C and F), $\hat{O}_2 \rightarrow \hat{C}_2$ seemed unaffected by NPPB (see fits to the distributions of open burst durations in 20 μM NPPB; Fig. 5 D), whereas rate $\hat{O}_1 \rightarrow \hat{C}_1$ reflects K1250A closing rate in 210 μM NPPB (Fig. 4 B). The rates in the top tier of the full scheme were chosen to yield the above compound rates in the presence of 210 μM NPPB.

Permeation effects of NPPB (Fig. 12 A, right) are modeled as simple voltage- and dose-dependent pore block and assumed instantaneous compared with gating effects. Thus, apparent unitary conductance (g) is approximated by the Boltzmann equation with parameters printed (g_0, control unitary conductance; T, temperature in Kelvin; $R = 8.31\ \text{J} \cdot \text{mol}^{-1} \cdot \text{K}^{-1}$; $F = 96{,}500\ \text{C} \cdot \text{mol}^{-1}$; $K_d(0)$ and z were chosen to best match fractional block measured at −120 and +60 mV, at which the majority of our dataset was obtained).

The predictions of this simplified model were verified by calculating macroscopic current time courses corresponding to all the experimental protocols tested in Figs. 2–4 and 6 and 7, as well as by simulating single-channel dwell-time sequences for all the conditions tested in Figs. 5 and 6 F. Macroscopic and single-channel traces were analyzed exactly as the corresponding experimental traces, and results are summarized in Fig. 12 (B–L). The predictions of the model were found to be in excellent agreement with our experimental observations. Indeed, the model faithfully reproduced (a) robust stimulation of WT P_o as reflected by a discrepancy between fractional effects on steady-state macroscopic and unitary currents (Fig. 12, B and C; compare to Figs. 2, A, B, and E, and 6, A and B) and current overshoots upon rapid removal of NPPB (Fig. 12 E; compare to Figs. 3 D and 6 D); (b) slowing of WT (hydrolytic) macroscopic closing rate (Fig. 12 D; compare to Figs. 3, A and C, and 6 C); (c) acceleration of WT macroscopic opening rate (Fig. 12 E; compare to Figs. 3 F and 6 D); (d) shortening and prolongation, respectively, of steady-state single-channel mean closed (interburst) and open (burst) durations (Fig. 12, F and H; compare to Figs. 5 B and 6 F), the latter being caused by a slowed rate $\hat{O}_1 \rightarrow \hat{O}_2$ (Fig. 12 G; compare to Fig. 5, C and D); (e) accelerated closing rate of the nonhydrolytic K1250A mutant (Fig. 12 I; compare to Figs. 4, A and B, and 6 E), but (f) lack of effect on the P_o of this channel (Fig. 12 J; compare to Fig. 4, C and D), (g) observed apparent affinities of the NPPB gating effects (Fig. 12 K; compare to Fig. 10), as well as (h) extremely efficient stimulation of low P_o mutants such as ΔF508 (Fig. 12 L; compare to Fig. 7; also compare to Fig. 8). Thus, our simplified model captures most key features of the complex effects of NPPB on CFTR function. Indeed, the only feature

the model does not account for is the observed slight voltage dependence of the stimulatory efficiency: 210 μM NPPB affected both opening and closing rates by approximately fourfold at −120 mV, but only by approximately threefold at +60 mV. This small difference is little apparent when the control (unstimulated) P_o is high. However, for low starting P_o values, NPPB-induced changes in the opening and closing rate affect P_o in a multiplicative manner, predicting an ∼16-fold stimulation at −120 mV, but only ∼9-fold at +60 mV, as found for the low P_o ΔF508 mutant (Fig. 7 D). This feature could be accounted for by assuming a slight voltage dependence of NPPB binding at the gating site; for instance, K_d could be ∼80 μM at −120 mV but closer to ∼100 μM at +60 mV.

In conclusion, our analysis has identified two strategic intervention points in the CFTR gating cycle to robustly stimulate P_o: stabilizing the transition state for opening, or slowing the ATP hydrolysis step. Both strategies uniquely rely on a nonequilibrium gating cycle. We have further identified a compound that is capable of exerting both effects. Identifying the NPPB gating site would be an exciting further step toward rational development of new nonblocking NPPB derivatives that stimulate CFTR gating with improved affinity, specificity, and/or potency. Such drugs—in combination with a suitable "corrector" compound to mend the folding defect and thermal instability of ΔF508 CFTR (Wang et al., 2011; Rabeh et al., 2012)—could provide pharmacological treatment for >90% of CF patients carrying at least one ΔF508 allele.

We thank David Gadsby and Paola Vergani for critical review and discussions.

This work is supported by National Institutes of Health grant R01-DK051767, MTA Lendület grant LP2012-39/2012, and an International Early Career Scientist grant from the Howard Hughes Medical Institute to L. Csanády.

The authors have no conflicting financial interests.

Edward N. Pugh Jr. served as editor.

Submitted: 19 August 2013
Accepted: 19 December 2013

REFERENCES

Ai, T., S.G. Bompadre, Y. Sohma, X.H. Wang, M. Li, and T.C. Hwang. 2004. Direct effects of 9-anthracene compounds on cystic fibrosis transmembrane conductance regulator gating. *Pflugers Arch.* 449:88–95. http://dx.doi.org/10.1007/s00424-004-1317-y

Aleksandrov, L., A.A. Aleksandrov, X.B. Chang, and J.R. Riordan. 2002. The first nucleotide binding domain of cystic fibrosis transmembrane conductance regulator is a site of stable nucleotide interaction, whereas the second is a site of rapid turnover. *J. Biol. Chem.* 277:15419–15425. http://dx.doi.org/10.1074/jbc.M111713200

Aleksandrov, A.A., L. Cui, and J.R. Riordan. 2009. Relationship between nucleotide binding and ion channel gating in cystic fibrosis transmembrane conductance regulator. *J. Physiol.* 587:2875–2886. http://dx.doi.org/10.1113/jphysiol.2009.170258

Aller, S.G., J. Yu, A. Ward, Y. Weng, S. Chittaboina, R.P. Zhuo, P.M. Harrell, Y.T. Trinh, Q.H. Zhang, I.L. Urbatsch, and G. Chang. 2009. Structure of P-glycoprotein reveals a molecular basis for polyspecific drug binding. *Science.* 323:1718–1722. http://dx.doi.org/10.1126/science.1168750

Bai, Y.H., M. Li, and T.C. Hwang. 2011. Structural basis for the channel function of a degraded ABC transporter, CFTR (ABCC7). *J. Gen. Physiol.* 138:495–507. http://dx.doi.org/10.1085/jgp.201110705

Basso, C., P. Vergani, A.C. Nairn, and D.C. Gadsby. 2003. Prolonged nonhydrolytic interaction of nucleotide with CFTR's NH_2-terminal nucleotide binding domain and its role in channel gating. *J. Gen. Physiol.* 122:333–348. http://dx.doi.org/10.1085/jgp.200308798

Bear, C.E., C.H. Li, N. Kartner, R.J. Bridges, T.J. Jensen, M. Ramjeesingh, and J.R. Riordan. 1992. Purification and functional reconstitution of the cystic fibrosis transmembrane conductance regulator (CFTR). *Cell.* 68:809–818. http://dx.doi.org/10.1016/0092-8674(92)90155-6

Bompadre, S.G., Y. Sohma, M. Li, and T.C. Hwang. 2007. G551D and G1349D, two CF-associated mutations in the signature sequences of CFTR, exhibit distinct gating defects. *J. Gen. Physiol.* 129:285–298. http://dx.doi.org/10.1085/jgp.200609667

Chen, T.Y., and T.C. Hwang. 2008. CLC-0 and CFTR: chloride channels evolved from transporters. *Physiol. Rev.* 88:351–387. http://dx.doi.org/10.1152/physrev.00058.2006

Chen, J.H., Z.W. Cai, and D.N. Sheppard. 2009. Direct sensing of intracellular pH by the cystic fibrosis transmembrane conductance regulator (CFTR) Cl^- channel. *J. Biol. Chem.* 284:35495–35506. http://dx.doi.org/10.1074/jbc.M109.072678

Cheng, S.H., R.J. Gregory, J. Marshall, S. Paul, D.W. Souza, G.A. White, C.R. O'Riordan, and A.E. Smith. 1990. Defective intracellular transport and processing of CFTR is the molecular basis of most cystic fibrosis. *Cell.* 63:827–834. http://dx.doi.org/10.1016/0092-8674(90)90148-8

Colquhoun, D., and F.J. Sigworth. 1995. Fitting and statistical analysis of single-channel records. *In* Single Channel Recording. B. Sakmann and E. Neher, editors. Plenum Press, New York. 483–587.

Csanády, L. 2000. Rapid kinetic analysis of multichannel records by a simultaneous fit to all dwell-time histograms. *Biophys. J.* 78:785–799. http://dx.doi.org/10.1016/S0006-3495(00)76636-7

Csanády, L. 2006. Statistical evaluation of ion-channel gating models based on distributions of log-likelihood ratios. *Biophys. J.* 90:3523–3545. http://dx.doi.org/10.1529/biophysj.105.075135

Csanády, L., K.W. Chan, D. Seto-Young, D.C. Kopsco, A.C. Nairn, and D.C. Gadsby. 2000. Severed channels probe regulation of gating of cystic fibrosis transmembrane conductance regulator by its cytoplasmic domains. *J. Gen. Physiol.* 116:477–500. http://dx.doi.org/10.1085/jgp.116.3.477

Csanády, L., K.W. Chan, A.C. Nairn, and D.C. Gadsby. 2005. Functional roles of nonconserved structural segments in CFTR's NH_2-terminal nucleotide binding domain. *J. Gen. Physiol.* 125:43–55. http://dx.doi.org/10.1085/jgp.200409174

Csanády, L., A.C. Nairn, and D.C. Gadsby. 2006. Thermodynamics of CFTR channel gating: A spreading conformational change initiates an irreversible gating cycle. *J. Gen. Physiol.* 128:523–533. http://dx.doi.org/10.1085/jgp.200609558

Csanády, L., P. Vergani, and D.C. Gadsby. 2010. Strict coupling between CFTR's catalytic cycle and gating of its Cl^- ion pore revealed by distributions of open channel burst durations. *Proc. Natl. Acad. Sci. USA.* 107:1241–1246. http://dx.doi.org/10.1073/pnas.0911061107

Dawson, R.J.P., and K.P. Locher. 2006. Structure of a bacterial multidrug ABC transporter. *Nature.* 443:180–185. http://dx.doi.org/10.1038/nature05155

Gadsby, D.C., P. Vergani, and L. Csanády. 2006. The ABC protein turned chloride channel whose failure causes cystic fibrosis. *Nature.* 440:477–483. http://dx.doi.org/10.1038/nature04712

Gunderson, K.L., and R.R. Kopito. 1994. Effects of pyrophosphate and nucleotide analogs suggest a role for ATP hydrolysis in cystic fibrosis transmembrane regulator channel gating. *J. Biol. Chem.* 269:19349–19353.

Gunderson, K.L., and R.R. Kopito. 1995. Conformational states of CFTR associated with channel gating: the role ATP binding and hydrolysis. *Cell.* 82:231–239. http://dx.doi.org/10.1016/0092-8674(95)90310-0

Hohl, M., C. Briand, M.G. Grütter, and M.A. Seeger. 2012. Crystal structure of a heterodimeric ABC transporter in its inward-facing conformation. *Nat. Struct. Mol. Biol.* 19:395–402. http://dx.doi.org/10.1038/nsmb.2267

Hwang, T.C., and D.N. Sheppard. 2009. Gating of the CFTR Cl^- channel by ATP-driven nucleotide-binding domain dimerisation. *J. Physiol.* 587:2151–2161. http://dx.doi.org/10.1113/jphysiol.2009.171595

Ishihara, H., and M.J. Welsh. 1997. Block by MOPS reveals a conformation change in the CFTR pore produced by ATP hydrolysis. *Am. J. Physiol.* 273:C1278–C1289.

Jackson, M.B., B.S. Wong, C.E. Morris, H. Lecar, and C.N. Christian. 1983. Successive openings of the same acetylcholine receptor channel are correlated in open time. *Biophys. J.* 42:109–114. http://dx.doi.org/10.1016/S0006-3495(83)84375-6

Jih, K.Y., and T.C. Hwang. 2013. Vx-770 potentiates CFTR function by promoting decoupling between the gating cycle and ATP hydrolysis cycle. *Proc. Natl. Acad. Sci. USA.* 110:4404–4409. http://dx.doi.org/10.1073/pnas.1215982110

Jih, K.Y., M. Li, T.C. Hwang, and S.G. Bompadre. 2011. The most common cystic fibrosis-associated mutation destabilizes the dimeric state of the nucleotide-binding domains of CFTR. *J. Physiol.* 589:2719–2731. http://dx.doi.org/10.1113/jphysiol.2010.202861

Jih, K.Y., Y. Sohma, and T.C. Hwang. 2012a. Nonintegral stoichiometry in CFTR gating revealed by a pore-lining mutation. *J. Gen. Physiol.* 140:347–359. http://dx.doi.org/10.1085/jgp.201210834

Jih, K.Y., Y. Sohma, M. Li, and T.C. Hwang. 2012b. Identification of a novel post-hydrolytic state in CFTR gating. *J. Gen. Physiol.* 139:359–370. http://dx.doi.org/10.1085/jgp.201210789

Karpowich, N., O. Martsinkevich, L. Millen, Y.R. Yuan, P.L. Dai, K. MacVey, P.J. Thomas, and J.F. Hunt. 2001. Crystal structures of the MJ1267 ATP binding cassette reveal an induced-fit effect at the ATPase active site of an ABC transporter. *Structure.* 9:571–586. http://dx.doi.org/10.1016/S0969-2126(01)00617-7

Kirk, K.L., and W. Wang. 2011. A unified view of cystic fibrosis transmembrane conductance regulator (CFTR) gating: combining the allosterism of a ligand-gated channel with the enzymatic activity of an ATP-binding cassette (ABC) transporter. *J. Biol. Chem.* 286:12813–12819. http://dx.doi.org/10.1074/jbc.R111.219634

Locher, K.P. 2009. Structure and mechanism of ATP-binding cassette transporters. *Philos. Trans. R. Soc. Lond. B Biol. Sci.* 364:239–245. http://dx.doi.org/10.1098/rstb.2008.0125

Miki, H., Z. Zhou, M. Li, T.C. Hwang, and S.G. Bompadre. 2010. Potentiation of disease-associated cystic fibrosis transmembrane conductance regulator mutants by hydrolyzable ATP analogs. *J. Biol. Chem.* 285:19967–19975. http://dx.doi.org/10.1074/jbc.M109.092684

Moody, J.E., L. Millen, D. Binns, J.F. Hunt, and P.J. Thomas. 2002. Cooperative, ATP-dependent association of the nucleotide binding cassettes during the catalytic cycle of ATP-binding cassette transporters. *J. Biol. Chem.* 277:21111–21114. http://dx.doi.org/10.1074/jbc.C200228200

Norimatsu, Y., A. Ivetac, C. Alexander, N. O'Donnell, L. Frye, M.S.P. Sansom, and D.C. Dawson. 2012. Locating a plausible binding site for an open-channel blocker, GlyH-101, in the pore of the cystic fibrosis transmembrane conductance regulator. *Mol. Pharmacol.* 82:1042–1055. http://dx.doi.org/10.1124/mol.112.080267

O'Sullivan, B.P., and S.D. Freedman. 2009. Cystic fibrosis. *Lancet.* 373:1891–1904. http://dx.doi.org/10.1016/S0140-6736(09)60327-5

Okiyoneda, T., H. Barrière, M. Bagdány, W.M. Rabeh, K. Du, J. Höhfeld, J.C. Young, and G.L. Lukacs. 2010. Peripheral protein quality control removes unfolded CFTR from the plasma membrane. *Science.* 329:805–810. http://dx.doi.org/10.1126/science.1191542

Rabeh, W.M., F. Bossard, H.J. Xu, T. Okiyoneda, M. Bagdany, C.M. Mulvihill, K. Du, S. di Bernardo, Y. Liu, L. Konermann, et al. 2012. Correction of both NBD1 energetics and domain interface is required to restore ΔF508 CFTR folding and function. *Cell.* 148:150–163. http://dx.doi.org/10.1016/j.cell.2011.11.024

Ramjeesingh, M., C. Li, E. Garami, L.J. Huan, K. Galley, Y. Wang, and C.E. Bear. 1999. Walker mutations reveal loose relationship between catalytic and channel-gating activities of purified CFTR (cystic fibrosis transmembrane conductance regulator). *Biochemistry.* 38:1463–1468. http://dx.doi.org/10.1021/bi982243y

Ramsey, B.W., J. Davies, N.G. McElvaney, E. Tullis, S.C. Bell, P. Drevínek, M. Griese, E.F. McKone, C.E. Wainwright, M.W. Konstan, et al. VX08-770-102 Study Group. 2011. A CFTR potentiator in patients with cystic fibrosis and the G551D mutation. *N. Engl. J. Med.* 365:1663–1672. http://dx.doi.org/10.1056/NEJMoa1105185

Riordan, J.R., J.M. Rommens, B. Kerem, N. Alon, R. Rozmahel, Z. Grzelczak, J. Zielenski, S. Lok, N. Plavsic, J.L. Chou, et al. 1989. Identification of the cystic fibrosis gene: cloning and characterization of complementary DNA. *Science.* 245:1066–1073. http://dx.doi.org/10.1126/science.2475911

Serohijos, A.W.R., T. Hegedus, A.A. Aleksandrov, L. He, L. Cui, N.V. Dokholyan, and J.R. Riordan. 2008. Phenylalanine-508 mediates a cytoplasmic-membrane domain contact in the CFTR 3D structure crucial to assembly and channel function. *Proc. Natl. Acad. Sci. USA.* 105:3256–3261. http://dx.doi.org/10.1073/pnas.0800254105

Smith, P.C., N. Karpowich, L. Millen, J.E. Moody, J. Rosen, P.J. Thomas, and J.F. Hunt. 2002. ATP binding to the motor domain from an ABC transporter drives formation of a nucleotide sandwich dimer. *Mol. Cell.* 10:139–149. http://dx.doi.org/10.1016/S1097-2765(02)00576-2

Szollosi, A., P. Vergani, and L. Csanády. 2010. Involvement of F1296 and N1303 of CFTR in induced-fit conformational change in response to ATP binding at NBD2. *J. Gen. Physiol.* 136:407–423. http://dx.doi.org/10.1085/jgp.201010434

Tabcharani, J.A., X.B. Chang, J.R. Riordan, and J.W. Hanrahan. 1991. Phosphorylation-regulated Cl^- channel in CHO cells stably expressing the cystic fibrosis gene. *Nature.* 352:628–631. http://dx.doi.org/10.1038/352628a0

Tsai, M.F., H. Shimizu, Y. Sohma, M. Li, and T.C. Hwang. 2009. State-dependent modulation of CFTR gating by pyrophosphate. *J. Gen. Physiol.* 133:405–419. http://dx.doi.org/10.1085/jgp.200810186

Tsai, M.F., M. Li, and T.C. Hwang. 2010. Stable ATP binding mediated by a partial NBD dimer of the CFTR chloride channel. *J. Gen. Physiol.* 135:399–414. http://dx.doi.org/10.1085/jgp.201010399

Van Goor, F., S. Hadida, P.D.J. Grootenhuis, B. Burton, D. Cao, T. Neuberger, A. Turnbull, A. Singh, J. Joubran, A. Hazlewood, et al. 2009. Rescue of CF airway epithelial cell function in vitro by a CFTR potentiator, VX-770. *Proc. Natl. Acad. Sci. USA.* 106:18825–18830. http://dx.doi.org/10.1073/pnas.0904709106

Verdon, G., S.V. Albers, N. van Oosterwijk, B.W. Dijkstra, A.J. Driessen, and A.M. Thunnissen. 2003. Formation of the productive ATP-Mg2+-bound dimer of GlcV, an ABC-ATPase from Sulfolobus solfataricus. *J. Mol. Biol.* 334:255–267. http://dx.doi.org/10.1016/j.jmb.2003.08.065

Vergani, P., A.C. Nairn, and D.C. Gadsby. 2003. On the mechanism of MgATP-dependent gating of CFTR Cl^- channels. *J. Gen. Physiol.* 121:17–36. http://dx.doi.org/10.1085/jgp.20028673

Vergani, P., S.W. Lockless, A.C. Nairn, and D.C. Gadsby. 2005. CFTR channel opening by ATP-driven tight dimerization of its nucleotide-binding domains. *Nature*. 433:876–880. http://dx.doi.org/10.1038/nature03313

Walsh, K.B., and C.M. Wang. 1998. Arylaminobenzoate block of the cardiac cyclic AMP-dependent chloride current. *Mol. Pharmacol.* 53:539–546.

Wang, W., G. Li, J.P. Clancy, and K.L. Kirk. 2005. Activating cystic fibrosis transmembrane conductance regulator channels with pore blocker analogs. *J. Biol. Chem.* 280:23622–23630. http://dx.doi.org/10.1074/jbc.M503118200

Wang, W., J.P. Wu, K. Bernard, G. Li, G.Y. Wang, M.O. Bevensee, and K.L. Kirk. 2010. ATP-independent CFTR channel gating and allosteric modulation by phosphorylation. *Proc. Natl. Acad. Sci. USA.* 107:3888–3893. http://dx.doi.org/10.1073/pnas.0913001107

Wang, W., G.O. Okeyo, B.L. Tao, J.S. Hong, and K.L. Kirk. 2011. Thermally unstable gating of the most common cystic fibrosis mutant channel (ΔF508): "rescue" by suppressor mutations in nucleotide binding domain 1 and by constitutive mutations in the cytosolic loops. *J. Biol. Chem.* 286:41937–41948. http://dx.doi.org/10.1074/jbc.M111.296061

Wangemann, P., M. Wittner, A. Di Stefano, H.C. Englert, H.J. Lang, E. Schlatter, and R. Greger. 1986. Cl(-)-channel blockers in the thick ascending limb of the loop of Henle. Structure activity relationship. *Pflugers Arch.* 407:S128–S141. http://dx.doi.org/10.1007/BF00584942

Ward, A., C.L. Reyes, J. Yu, C.B. Roth, and G. Chang. 2007. Flexibility in the ABC transporter MsbA: Alternating access with a twist. *Proc. Natl. Acad. Sci. USA.* 104:19005–19010. http://dx.doi.org/10.1073/pnas.0709388104

Zhang, Z.R., S. Zeltwanger, and N.A. McCarty. 2000. Direct comparison of NPPB and DPC as probes of CFTR expressed in Xenopus oocytes. *J. Membr. Biol.* 175:35–52. http://dx.doi.org/10.1007/s002320001053

Zhou, J.J., M.S. Li, J.S. Qi, and P. Linsdell. 2010. Regulation of conductance by the number of fixed positive charges in the intracellular vestibule of the CFTR chloride channel pore. *J. Gen. Physiol.* 135:229–245. http://dx.doi.org/10.1085/jgp.200910327